Aalto University
School of Science
Degree Programme in Engineering Physics

Antti Moisio

Quasiparticle density in hybrid single electron turnstiles

Master's Thesis
Helsinki, January 17, 2017

Supervisor: Professor Jukka Pekola
Advisor: D.Sc. (Tech.) Joonas Peltonen

Aalto University
School of Science
Degree Programme in Engineering Physics

ABSTRACT OF
MASTER'S THESIS

Author: Antti Moisio

Title:
Quasiparticle density in hybrid single electron turnstiles

Date: January 17, 2017 **Pages:** 54

Major: Engineering Physics **Code:** SCI3056

Supervisor: Professor Jukka Pekola

Advisor: D.Sc. (Tech.) Joonas Peltonen

The SI unit ampere will be tied to an agreed value of the elementary charge within few years. With this redefinition, the ampere can be realised by controlled transfer of individual electrons at a constant frequency. This provides a direct frequency-to-current conversion.

One promising candidate for a new current standard is the SINIS turnstile, which consists of a small normal metal island that is connected to two superconducting leads via insulating barriers. A major problem for these types of devices is the existence of nonequilibrium quasiparticles, which are generated during operation of the device. These quasiparticles may tunnel through the insulating barriers causing excess current.

In order to reduce the number of quasiparticles in the vicinity of the junctions, the geometry of the leads must be optimised. The quasiparticle density can be significantly reduced by designing the leads in such a way that the quasiparticles may effectively diffuse away from the tunnel junction. In this work, we have studied a simple diffusion model for quasiparticle transport and fabricated SINIS turnstiles with varying lead thicknesses.

In this work, we have fabricated devices where the normal metal island is either Cu or AlMn. The Mn suppresses the superconducting properties of Al, resulting in a normal metal island that can be oxidised in order to fabricate tunnel junctions for devices with very thick superconducting leads.

We were able to demonstrate that AlMn based devices can be indeed fabricated and that their charging energy can exceed the superconducting gap, which is essential in order to suppress several error mechanisms. However, we were not able to verify whether having thicker leads has a significant effect on the quasiparticle density.

Keywords: ampere, superconductivity, SINIS turnstile, quasiparticles, lead geometry

Language: English

Aalto-yliopisto
Perustieteiden korkeakoulu
Tietotekniikan koulutusohjelma

DIPLOMITYÖN
TIIVISTELMÄ

Tekijä:	Antti Moisio		
Työn nimi:	Kvasipartikkelitiheys yhden elektronin hybridikiertopumpuissa		
Päiväys:	17. tammikuuta 2017	**Sivumäärä:**	54
Pääaine:	Teknillinen fysiikka	**Koodi:**	SCI3056
Valvoja:	Professori Jukka Pekola		
Ohjaaja:	TkT Joonas Peltonen		

SI-järjestelmän perusyksikköihin kuuluva ampeeri tullaan lähitulevaisuudessa määrittelemään uudestaan kiinnittämällä alkeisvarauksen arvo. Uuden määritelmän perusteella ampeeri voidaan toteuttaa siirtämällä yksittäisiä elektroneja kiinteällä taajuudella, mikä tarjoaa suoran taajuus-virta-muunnoksen.

Eräs lupaava kandidaatti uudeksi virtastandardiksi on SINIS-hybridikiertompumppu, joka koostuu pienestä normaalimetallisaarekkeesta, joka on yhdistetty kahteen suprajohtavaan johtimeen siten, että metallien välissä on eristekerros. Eräs suurimmista ongelmista pumpuille on pumppaksen aikana syntyvät kvasipartikkelit, jotka voivat tunneloitua eristekerroksen läpi kasvattaen laitteen läpi kulkevaa sähkövirtaa.

Jotta kvasipartikkelien lukumäärää tunneliliitosten läheisyydessä voidaan vähentää, on johdinten geometriaa optimoitava. Johtimet on suunniteltava siten, että kvasipartikkelit pääsevät tehokkaasti diffundoitumaan kauemmas liitoksista. Tässä diplomityössä kvasipartikkelien kulkeutumista tutkittiin yksinkertaisella diffuusiomallilla sekä valmistettiin hybridikiertopumppuja, joiden johdinten paksuus vaihteli.

Työssä valmistettujen pumppujen normaalimetalleina käytettiin joko kuparia tai mangaanilla seostettua alumiinia. Mangaani tukahduttaa alumiinin suprajohtavat ominaisuudet, jolloin tuloksena on normaalimetalli, jonka pinnalle voidaan kasvattaa oksidikerros, joka toimii pumpuissa saaren ja johtimet erottavana eristeenä, kun halutaan valmistaa laitteita, joissa on hyvin paksut johtimet.

Työssä osoitettiin, että alumiinin ja mangaanin seoksesta voidaan valmistaa hybridipumppuja, joiden varautumisenergia on suurempi kuin suprajohtavan alumiinin energia-aukko. Tämä on tärkeä ominaisuus, sillä näin saadaan estettyä tiettyjä keskeisiä virhemekanismeja. Työssä ei kuitenkaan saatu kokeellisesti vahvistettua sitä, vaikuttaako johdinten paksuus merkittävästi kvasipartikkelitiheyteen.

Asiasanat:	ampeeri, suprajohtavuus, SINIS-kääntöportti, kvasipartikkelit, johdingeometria
Kieli:	Englanti

Contents

1 Acknowledgements

I would like to thank my supervisor, Professor Jukka Pekola for giving me the opportunity to work in the PICO group of the Department of Applied Physics in Aalto University.

I would also like to thank my instructor, Dr. Sc. (Tech.) Joonas Peltonen for his help on the practical work ranging from sample fabrication to the actual measurements, as well as his detailed comments on the earlier version of this thesis.

I wish to thank all the members of the PICO group with whom I've had the pleasure to work with over the past few years.

I also wish to thank OtaNano for providing the facilities necessary to conduct the research presented in this thesis.

Finally, I would like to thank my fiancé Aino for her invaluable support during the writing of this thesis.

Helsinki, January 17, 2017
Antti Moisio

2 Introduction

When measuring any physical quantity, the whole process boils down to a comparison. If one is using a ruler as the instrument, then the value to which the distance between two given points is compared, is the distance between two ticks of the ruler. The distance between the ticks of the ruler then needs to be compared to some other reference and so forth. In the SI system, the ultimate reference for length is the distance traveled by light in vacuum in a certain time interval. Thus, the definition of the SI unit of length, the meter, is based on a constant of Nature, namely the speed of light c [1].

Currently, four of the seven base units of the SI system are based on constants of Nature. In addition to the meter, these are the second, kelvin and candela. The kilogram is based on the mass of an artefact, which is susceptible to drifting over time. Furthermore, the definitions of the mole and the ampere are also tied to this artifact since the mole is defined as the number of atoms in 12 grams of ^{12}C whereas the definition of the ampere is even more convoluted:

"The ampere is that constant current which, if maintained in two straight parallel conductors of infinite length, of negligible circular cross-section, and placed 1 metre apart in vacuum, would produce between these conductors a force equal to 2×10^{-7} newton per metre of length." [1]

This definition is problematic in several ways. As mentioned earlier, it ties the ampere to the definition of the kilogram through the unit of force, the newton. Secondly, due to geometrical constraints, the ampere has not been directly realised at an uncertainty level lower than a few parts per 10^6 [2]. Perhaps a bit surprisingly, the main limitation is not the geometry of the wires since the force between wires of any shape can be exactly predicted using Biot-Savart's Law [3] and the Lorentz Force law. Instead, the lack of sufficient knowledge about the current distribution within the wires restricts the accuracy [4].

In the upcoming revision of the SI units, the ampere will be tied to the elementary charge e while the mole will be tied directly to the Avogadro number. Furthermore, the definitions of kilogram and kelvin will also be tied to constants of Nature, namely the Planck's constant h and Boltzmann constant k_B, respectively.

Since its advent in the early 1900s, quantum mechanics has been used to explain and predict numerous fascinating phenomena. From the point of view of electrical metrology, two phenomena are of crucial importance. The first one is the Josephson effect [5], where the average voltage across a junction, consisting of two superconductors separated by an insulating layer, that is driven by an ac current at frequency f_J, is quantized and takes values $nhf_J/2e = nf_j/K_J$, where n is an integer and $K_J = 2e/h \approx 484$ THz/V is called the Josephson constant.

The second phenomenom is the Quantum Hall effect [6], which is the quantization of the resistance of a two-dimensional electron gas under a high magnetic field, where the resistance takes values $h/ne^2 = R_k/n$, where $R_k = h/e^2 \approx 25.8$ kΩ is called the von

Klitzing constant and n is an integer.

The two effects have been used to establish the standards for volt and ohm, respectively. With these standards, the ampere can be realised indirectly with smaller uncertainty [4]. However, this type of realisation wouldn't be practical since tracing electrical units to fundamental constants provides much higher accuracy.

As discussed above, the redefinition of ampere will be based on a fixed value of the elementary charge. Thus, one ampere can be realised by the controlled transport of N electrons at a fixed frequency f resulting in a current $I = Nef$ [7]. The most promising candidates for devices capable of such transfer are based on quantum mechanical tunneling, which is is yet another example of quantum phenomena being used for metrological purposes. Research on these so-called single electron sources has been active over the last few decades thanks to advances in nanofabrication techniques [8]. In this introduction, we will discuss normal metallic and hybrid (consisting of normal metallic and superconducting parts) devices in more detail. Fully superconducting devices have also been proposed [9, 10], in addition to devices based on semiconducting quantum dots [11–13].

Most single-electron devices transfer electrons between two conducting leads via an island in-between. Due to a phenomenom called Coulomb blockade [14], the island can usually be occupied by a small number, usually just one, excess electron. This also requires that the thermal energy of the electrons does not exceed the characteristic charging energy in these systems, which means that the experiments have to be carried out at very low temperatures.

The earliest single-electron current sources utilised several normal metal islands connected in series [15], and electrons were transported through the islands by controlling their electrostatic potential with external gate electrodes.

With fully normal metallic devices, suppression of so-called co-tunneling, where an electron tunnels from the source lead to the island while an electron simultaneously tunnels from the island to the drain lead, is of crucial importance. Errors caused by co-tunneling are reduced by connecting multiple islands in series. So far, the most accurate results for normal metallic devices have been achieved with a device consisting of seven tunnel junctions [16]. As the number of islands increases, operating the device becomes more difficult, which ultimately restricts the operating frequency. In the seven-junction pump, an accuracy of 1.5×10^{-8} was achieved, but the operating frequency was only 5.05 MHz, and the resulting current output was 0.8 pA, which is not high enough to establish a current standard. In a later experiment, a similiar device was used to establish the standard for capacitance [17].

In 2008, the hybrid single electron turnstile was introduced [18]. In this device, either the island or the leads are superconducting. The former device is called a NISIN turnstile whereas the latter is called a SINIS turnstile. The letters S, I and N refer to superconductor, insulator and normal metal, respectively. The energy gap in the density of states in a superconductor effectively suppresses cotunneling, leading to a much simpler device design, consisting of only a single island. This relatively simple structure allows several devices to be connected in parallel to increase the current output, as was demonstrated in 2009 [19]. Parallelisation of the devices is essential since it has been predicted, that

the current of aluminum-based devices is limited to around 10 pA [8], whereas a current output of the order of 100 pA is required for metrological applications.

A major problem for the accuracy of the turnstile are the non-equilibirum quasiparticles injected into the leads during turnstile operation. These quasiparticles consist of unpaired electrons in the superconductor that carry enough energy to overcome the Coulomb blockade, resulting in an excess current output, unless they are removed from the vicinity of the junctions. Several schemes for this have been suggested, such as normal metallic traps [20] or magnetic vortices [21]. In this thesis, we wish to study the effects of the thickness of the leads on the density of the quasiparticles in the framework of a simple diffusion model.

In addition to the realisation of the redefined ampere, single electron current sources can be used to conduct an experiment known as the quantum metrological triangle [22]. In such an experiment, the current produced by a single-electron device is fed through a resistor operating at one of the resistance plateaus related to the Quantum Hall effect while the voltage across the resistor is probed using an array of Josephson junctions. If the single electron device is operated at a frequency f_{SET} and the Josephson junction array is driven with an ac current at frequency f_J, then by using Ohm's law, one obtains

$$K_J R_K Q_{SET} = in \frac{f_J}{f_{SET}}, \tag{1}$$

where Q_{SET} is the amount of charge transfered in a single cycle of the single-electron current source and n and i are the indices of the Josephson voltage and Hall plateaux used, respectively. The right-hand side consists of a product of two integers and the ratio between two frequencies, which can be measured with extremely low uncertainty. Thus, the quantum metrological triangle acts as a consistency check for the fundamental physical constants e and h. Furthermore, since the right-hand size is dimensionless, it is independent of the chosen unit system.

This thesis is organized as follows: in the next section we will review the physics relevant to the SINIS turnstiles by briefly discussing superconductivity, followed by the basic physics of hybrid single electron transistors, including both stationary and time-dependent operation. Finally, we will discuss quasiparticle excitations in the turnstile in further detail. In the third section we will review the experimental techniques used to study the devices. We will give a brief overview of the sample fabrication process, followed by the description of the experimental setup and the measurement procedures. In the fourth section we will present the results of our measurements and in the fifth section we will discuss the results.

3 Theoretical background

3.1 Superconductivity

Superconductivity is a feature that some metals exhibit at below a material-dependent critical temperature. In a superconducting state, two striking features emerge. The first feature is the lack of electrical resistance, allowing electric currents to run without dissipation for extended periods of time [23]. For the work presented in this thesis, however, a more interesting feature is a temperature-dependent energy gap Δ in the density of states of the electrons.

Superconductivity is due to pairing of electrons of opposite momenta and spin via a phonon-mediated attractive interaction. [24] The electrons in a superconductor can be described by the following Hamiltonian [25]:

$$\hat{H} = \sum_{k\sigma} \varepsilon_k c^\dagger_{k\sigma} c_{k\sigma} + \sum_{kl} V_{kl} c^\dagger_{k\uparrow} c^\dagger_{-k\downarrow} c_{-l\downarrow} c_{l\uparrow}, \tag{2}$$

where $c_{k\sigma}$ and $c^\dagger_{k\sigma}$ are the fermionic annihilation and creation operators for electrons with momentum k and spin σ, ε_k are the energies of the single-particle states with momentum k and V_{kl} describes the interaction between electrons with momentum k and l.

Now define the operators $b_k = \langle c_{-k\downarrow} c_{k\uparrow} \rangle$ and $\delta_k = c_{-k\downarrow} c_{k\uparrow} - b_k$. Assuming that δ_k is small, we can expand equation (2) up to first order to obtain

$$\hat{H} = \sum_{k\sigma} \varepsilon_k c^\dagger_{k\sigma} c_{k\sigma} - \sum_k (\Delta_k c^\dagger_{k\uparrow} c^\dagger_{-k\downarrow} + \Delta^*_k c_{-k\downarrow} c_{k\uparrow} - \Delta_k b^*_k), \tag{3}$$

where $\Delta_k = -\sum_l V_{kl} b_l$ is called the superconducting gap. Equation (3) can be simplified by introducing the operators

$$\begin{cases} c^\dagger_{k\uparrow} = v^*_k \gamma_{-k\downarrow} + u_k \gamma^\dagger_{k\uparrow} \\ c^\dagger_{-k\downarrow} = -v^*_k \gamma_{k\uparrow} + u_k \gamma^\dagger_{-k\downarrow} \end{cases} \tag{4}$$

and by choosing the coefficients v_k and u_k so that

$$\begin{cases} |u_k|^2 + |v_k|^2 = 1 \\ |v_k|^2 = \frac{1}{2}(1 - \frac{\varepsilon_k}{E_k}), \end{cases} \tag{5}$$

where $E_k = \sqrt{\varepsilon_k^2 + \Delta_k^2}$. With these conditions, inserting equation (4) into the Hamiltonian in equation (3) leads to

$$\hat{H} = \sum_{k\sigma} E_k \gamma^\dagger_{k\sigma} \gamma_{k\sigma} + constant \tag{6}$$

The constant in equation (6) may be ignored since we are only interested in changes in energy.

We will now calculate the density of states in a superconductor. We start by noting that close to the Fermi energy, the energies E_k do not depend on the momentum and we can thus drop the subscripts k. According to equation (6), we can describe excitations in superconductors as fermions created by $\gamma^\dagger$ that are in one-to-one correspondence with the standard electronic creation operator $c^\dagger$. Therefore we can then set $N_s(E)dE = N_n(\varepsilon)d\varepsilon$ because the number of electronic states must be equal to the number of quasiparticle states corresponding to the same energy. Since we are only considering fairly narrow energy ranges in the vicinity of the Fermi energy, we may consider the normal state density of states constant. Denoting this constant as N_0 we obtain

$$n_s(E) = N_0 \frac{d\varepsilon}{dE} = \frac{|E|}{\sqrt{\Delta^2 - E^2}} \tag{7}$$

for $|E| > \Delta$ and zero elsewhere.

3.2 Single-electron tunnelling

A tunnel junction is a structure consisting of two conducting electrodes with an insulating barrier between them. In such a structure, charge transport is achieved by quantum mechanical tunneling. As discussed in the introduction, the devices studied in this thesis contain junctions consisting of a normal metal (N) and a superconductor (S) separated by an insulator (I), or NIS junctions for short. They can be described with the following Hamiltonian

$$\hat{H} = \hat{H}_N + \hat{H}_S + \hat{H}_T. \tag{8}$$

The first two terms describe the electrons in the normal and superconducting electrodes. $\hat{H}_N$ has the form $\hat{H} = \sum_{k\sigma} \varepsilon_k a^\dagger_{k\sigma} a_{k\sigma}$, where $a^\dagger$ and a are the fermionic creation and annihilation operators for the normal metal, and $\hat{H}_S$ is the BCS Hamiltonian discussed earlier. The third term in equation (8) is the tunneling Hamiltonian, which can be written as $\hat{H}_T = \sum_{k\sigma} = t_{kq} c^\dagger_{q\sigma} a_{k\sigma} + h.c.$ [26]. The current flowing through the junction can be computed by constructing the corresponding operator. This is most conveniently done using the Heisenberg picture. We obtain

$$\hat{I} = e\frac{d}{dt}\hat{N}_N = \frac{ie}{\hbar}[\hat{H}, \hat{N}_N] = \frac{ie}{\hbar}[\hat{H}_T, \hat{N}_N], \tag{9}$$

where $\hat{N}_N = \sum_{k\sigma} a^\dagger_{k\sigma} a_{k\sigma}$ is the number of electrons in the normal metal. By calculating the expectation value $\langle I \rangle$ of the current operator, we obtain the single electron tunneling rates from the normal metal to the superconductor and vice versa. The result is

$$\Gamma_{N\to S}(\delta E) = \frac{1}{e^2 R_T} \int_{-\infty}^{\infty} dE n_S(E) f_N(E - \delta E)(1 - f_S(E)) \tag{10}$$

$$\Gamma_{S\to N}(\delta E) = \frac{1}{e^2 R_T} \int_{-\infty}^{\infty} dE n_S(E) f_S(E)(1 - f_N(E + \delta E)) \tag{11}$$

where e is the elementary charge, R_T is the tunneling resistance, n_s is the density of states in the superconductor and $f(E)$ is the Fermi-Dirac distribution function [26].

In addition to charge, the tunneling electrons also carry heat. The heat flow between the normal metal and superconductor can be calculated in a similiar manner as the tunneling rate, yielding

$$\dot{Q}_{N\to S} = \frac{1}{e^2 R_T}\int_{-\infty}^{\infty} dE E n_S(E) f_N(E-\delta E)(1-f_S(E)) \tag{12}$$

$$\dot{Q}_{S\to N} = \frac{1}{e^2 R_T}\int_{-\infty}^{\infty} dE E n_S(E) f_S(E)(1-f_N(E+\delta E)) \tag{13}$$

The subscripts N and S in equations (10)–(13) refer to normal metal and superconductor, respectively. As discussed above, the density of states in the normal metal close to the Fermi level may be considered constant and is thus included in the tunneling resistance. Due to the properties of the density of states of the superconductor and the Fermi-Dirac distribution, it can be shown with elementary algebra that the tunneling rates do not depend on the tunneling direction but only on the energy gain, i.e. $\Gamma_{N\to S}(\delta E) = \Gamma_{S\to N}(\delta E)$, and we can drop the subscripts.

In fig. 1 we have plotted a diagram of the electron occupations on both sides of the junction as well as the I-V curve of a single NIS junction at two different temperatures. A bias voltage across the junction shifts the Fermi energies of the two electrodess. At low temperatures the current is suppressed in the subgap regime since there are no available states in the superconductor around the Fermi energy of the normal metal.

Current in subgap voltages ($V_b \ll \Delta/e$) may also arise by various other mechanisms such as coupling to a high-temperature environment [27] or higher-order tunneling processes [28]. The leakage caused by absorption of photons from the environment can, under realistic approximations, be modeled by using an effective density of states

$$n_{eff} = \left|\mathrm{Re}\left(\frac{E/\Delta + i\gamma}{\sqrt{(E/\Delta+i\gamma)^2-1}}\right)\right|, \tag{14}$$

where the unitless γ is called the leakage parameter. With this density of states, the subgap current is approximately $I_{sg} \approx \gamma V/R_T$, which allows us to experimentally determine the parameter γ. In aluminum-based devices, it is usually in the range 10^{-5}–10^{-6} [29]. This environmentally activated tunneling can be reduced drastically with proper microwave shielding of the samples. [30]

3.3 The SINIS turnstile

A more complex device than a single tunnel junction, where single electron tunneling plays a pivotal role, is the single electron transistor (SET) [14]. It consists of a small conducting island connected to two leads via tunnel junctions. Furthermore, the island is also connected to a gate electrode, as shown in fig. 2. The SINIS turnstile is simply a biased SET, where a periodic gate drive V_g is applied to the capacitively coupled gate electrode.

We start our theoretical treatment by considering a static case, where the gate voltage is constant and derive an expression for the electrostatic energy of the island.

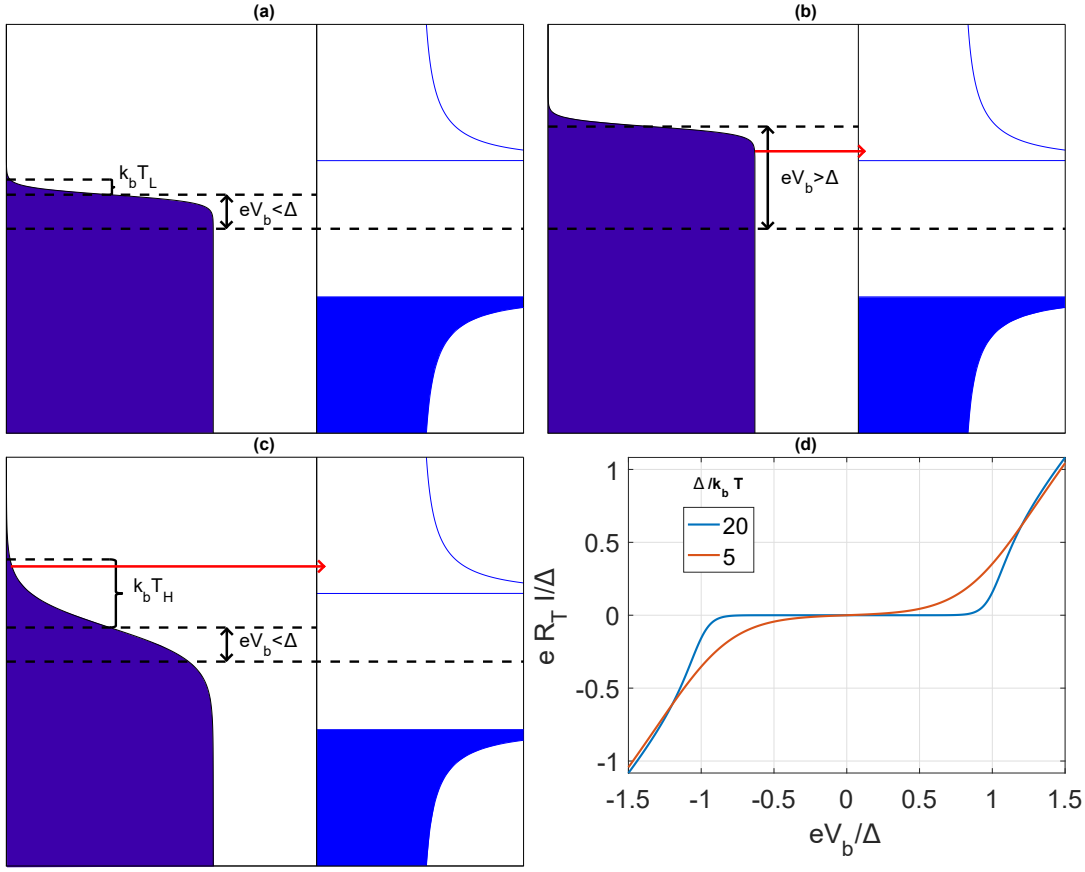

Figure 1: A schematic figure of electron transport in a NIS junction. In panel (a) the bias voltage is less than Δ/e and the current is suppressed. In panel (b) the bias voltage is higher than Δ/e and electrons may tunnel across the junction as indicated by the right-pointing arrow. In panel (c) the temperature of the normal metal is higher compared to panel (a), and electrons may tunnel across the junction even at low bias voltages. In panel (d) we have plotted the I-V characteristics of the junction at two different temperatures. We did not consider the temperature dependence of the gap since it is not significant for $T \lesssim T_c/3$.

From fig. 2 we can deduce that

$$\begin{cases} V_I = V_i - \frac{Q_i}{C_i} \\ \sum_i Q_i = -ne, \end{cases} \tag{15}$$

where V_I is the potential of the island and V_i and Q_i are the voltage and charge of each capacitor. Multiplying the first equation by C_iC_j yields

$$C_iC_jV_I = C_iC_j(V_i - \frac{Q_i}{C_i}) = (C_iV_i - Q_i)C_j, \tag{16}$$

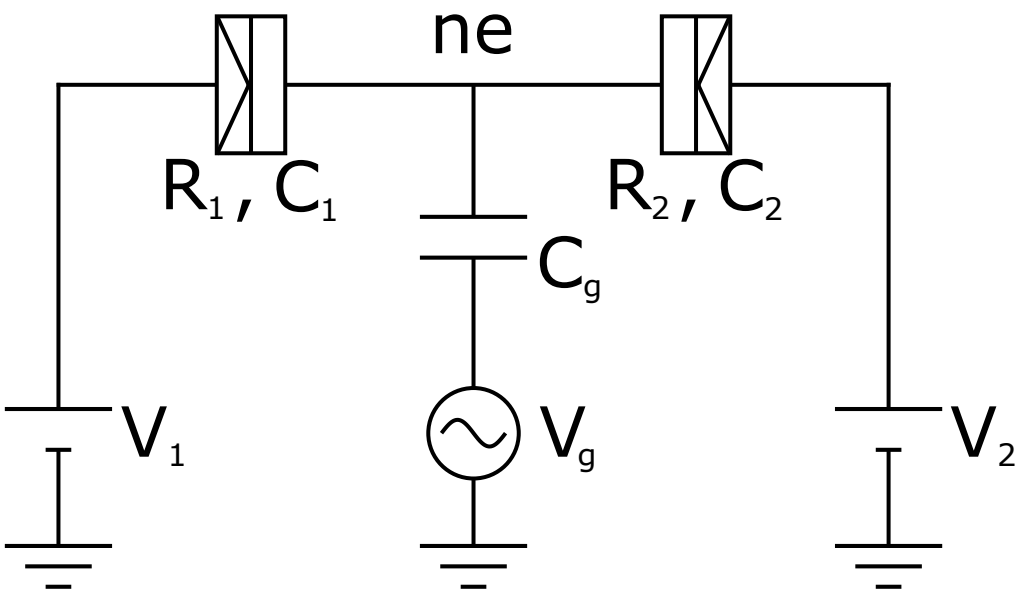

Figure 2: The single-electron transistor consists of a conducting island capacitively coupled to several voltage sources.

and summing over all indices and rearranging the terms finally yield for the charge of capacitor i

$$Q_i = C_i V_i + \frac{C_i}{C_\Sigma} e(n - n_g), \tag{17}$$

where the $C_\Sigma = \sum_i C_i$ is the total capacitance and

$$n_g = \sum_i \frac{C_i V_i}{e} \tag{18}$$

is called the gate offset. With the charges known, we can compute the energy stored in the circuit, which is defined as

$$E_{tot} = \sum_i \frac{Q_i^2}{2C_i} - Q_i V_i. \tag{19}$$

The first term describes the energy associated with the Coulomb repulsion of the charges on the capacitors while the second term is the energy supplied by the voltage sources. Substituting Q_i from equation (17) and keeping only the n-dependent part yields

$$E(n) = \frac{e^2}{2C_\Sigma}(n - n_g)^2 \equiv E_c(n - n_g)^2, \tag{20}$$

where $E_c = e^2/(2C_\Sigma)$ is called the charging energy. Thus, when the electron number on the island changes from n to $n \pm 1$, the change in the electrostatic energy is

$$\delta E^\pm = E(n) - E(n \pm 1) = \mp 2E_c(n - n_g \pm 1/2). \tag{21}$$

We still need to take into account the bias voltage. Therefore, the total change in energy when an electron tunnels through junction i is

$$\delta E^{\pm 0_i} = E(n) - E(n \pm 1) = \mp 2E_c(n - n_g \pm 1/2) \mp eV_i. \tag{22}$$

When considering charge transport through an SET, one has to take into account all the possible charge states. Let P_n be the probability of n excess electrons occupying the island. Then these probabilities evolve according to the master equation

$$\frac{d}{dt}P_n = -(\Gamma_{n,n-1} + \Gamma_{n,n+1})P_n + \Gamma_{n-1,n}P_{n-1} + \Gamma_{n+1,n}P_{n+1}, \tag{23}$$

where $\Gamma_{i,j}$ is the sum of all tunneling rates that change the charge on the island from i to j. In a steady state ($\frac{d}{dt}P_n = 0$) the master equation reduces to a system of linear equations and the corresponding current through junction i is then

$$I_i = -e\sum_n P(n)(\Gamma_{S\to N}(\delta E_i^+(n) - \Gamma_{N\to S}(\delta E_i^-(n)). \tag{24}$$

In fig. 3 we have plotted the current-voltage characteristics of a SINIS type single electron transistor for different values of n_g. For every n_g the current is suppressed in the sub-gap regime since in this regime the voltage sources do not provide enough energy to break the Cooper pairs. For $n_g = n + 1/2$, where n is an integer, we observe that the regime where the current is suppressed is the smallest. This is because in such a case, the charge states n and $n + 1$ have equal energy and hence as long as the voltage sources provide enough energy to break the Cooper pairs, electrons may tunnel from the leads to the island. On the other hand, when n_g is an integer, the regime of suppressed current is widest. This is because for integer values of n_g the change in energy, when n changes to $n \pm 1$, is the largest, as can be seen from equation (21).

3.4 Charge pumping with the SINIS turnstile

We will now turn our attention to the time-dependent case where the gate offset is driven sinusoidally, i.e. $n_g(t) = n_{g0} + A_g \sin(2\pi ft)$. We assume that the bias voltage is less than the gap energy so that dc current is suppressed during turnstile operation.

From equation (22) we can derive the threshold for an electron to tunnel to or from the island through each junction. For describing the basic operation of the turnstile, we only need to consider the thresholds for the charge states $n = 0$ and $n = 1$. The threshold for an electron to tunnel on the island via the left lead is

$$n_g = \frac{\Delta - eV_b}{2E_c} + \frac{1}{2}. \tag{25}$$

This threshold corresponds to the solid black line in fig. 4. The figure also shows the other single-electron tunneling thresholds between states $n = 0$ and $n = 1$. The driving is shown as the double-headed black arrow. We assume that the driving starts at $n_g = \frac{1}{2}$. As we increase the gate offset we will eventually reach the tunneling threshold $L(0 \to 1)$

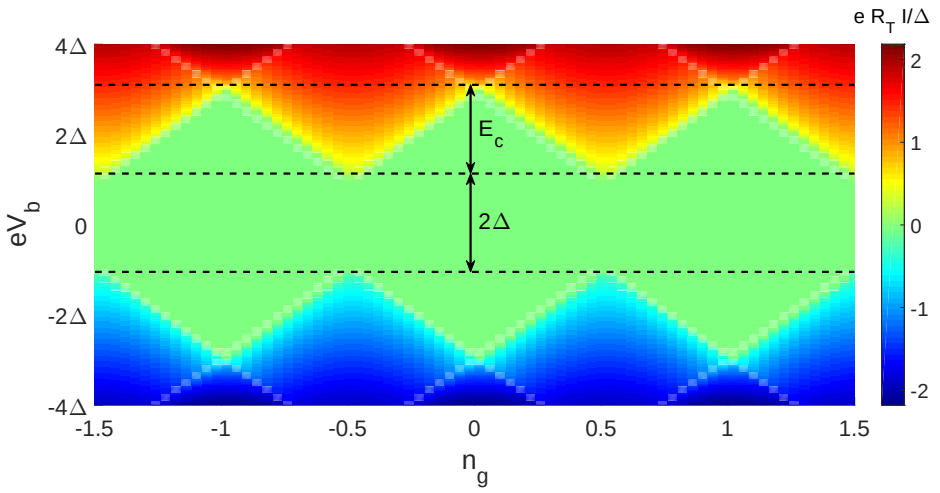

Figure 3: The dc current characteristics of a hybrid single electron transistor as a function of gate offset and bias voltage. In the calculation, we use $E_c = 2\Delta$.

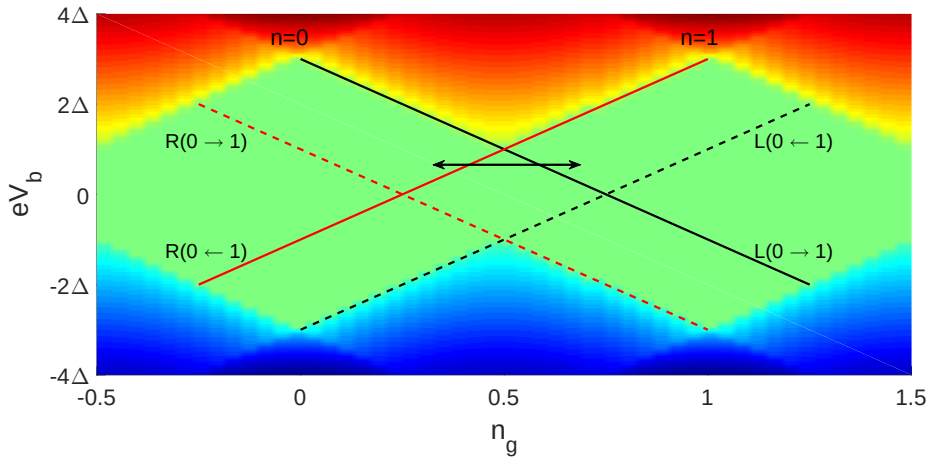

Figure 4: The operation of the SINIS turnstile. The solid and dashed lines correspond to various tunneling thresholds between charge states $n = 0$ and $n = 1$.

and an electron may tunnel through the left junction into the island. If we now start decreasing the gate offset until the solid red line [corresponding to $R(1 \to 0)$] is crossed, the electron will tunnel out from the island through the right junction, resulting in one electron being transfered through the device during one cycle of the gate drive, yielding an output current of ef. In fig. 5 we show a simulated current output of the device as a function of the drive parameters, namely the offset and the amplitude. It can be clearly seen that we obtain various stable current plateaus with varying current outputs. It can also be seen that the current output is periodic as a function of the gate offset with a

period of unity.

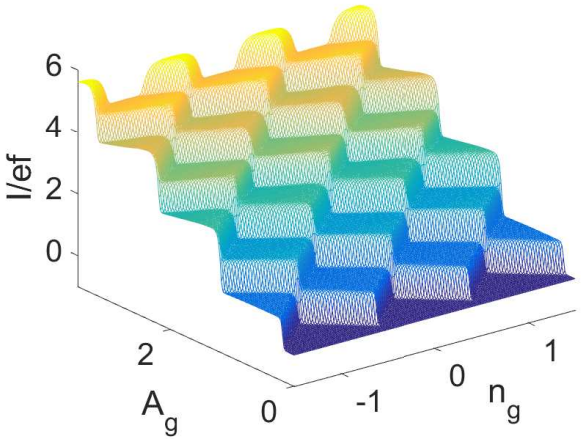

Figure 5: A simulation of the current output as a function of the driving amplitude and offset. We notice that the current output is periodic as a function of the gate offset with a period of unity. Various current plateaus with different current outputs can easily be distinguished.

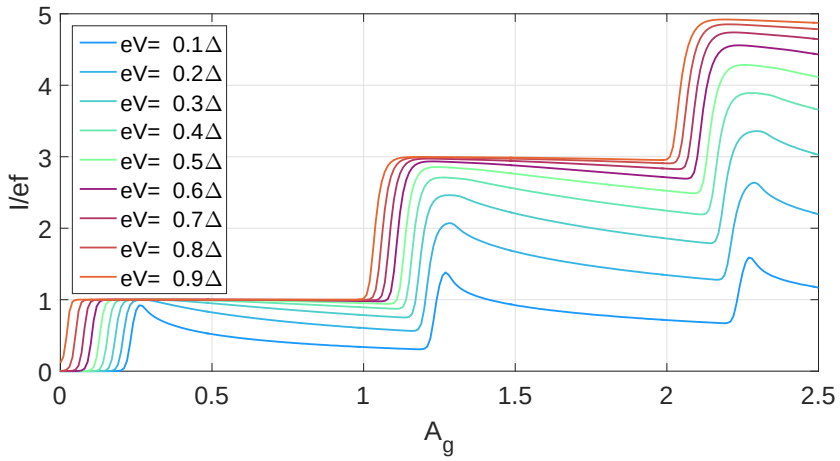

Figure 6: Simulated pumping curves for several bias voltages. The bias voltages in the legends indicate voltage per junction so the bias over the whole device is twice as high. The vertical axis displays the normalised current. The horizontal axis displays the amplitude of the pumping in units of of the normalised gate offset n_g. The gate offset is driven around the points $n_g = 1/2$ and the temperature used in the simulations is $40\Delta/k_B$ in the normal metal and $25\Delta/k_B$ in the superconductor.

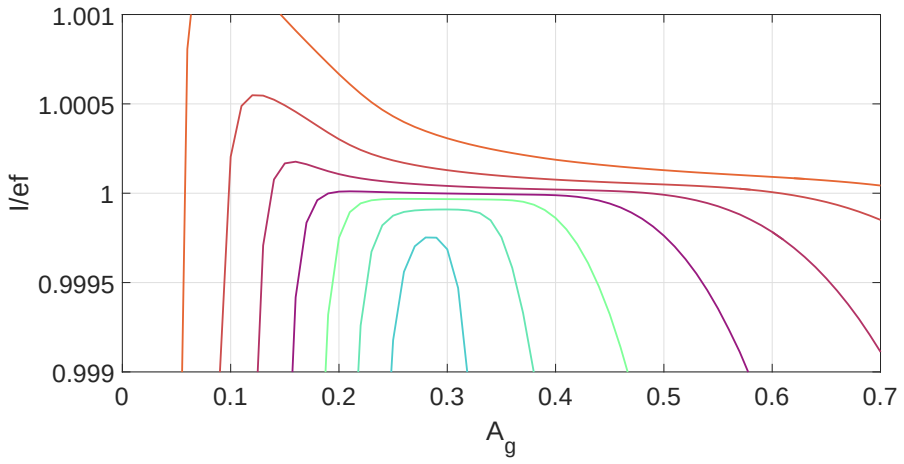

Figure 7: Same pumping curves as in fig. 6 on a zoomed scale. The colors correspond to the same biases as in the previous figure.

Figures 6 and 7 show simulations of the output current as a function of gate amplitude at several bias voltages. From the figure we can see that at lower biases, the current output starts decreasing at higher amplitudes before the sharp increase in current when reaching the second plateau, where $I = 3ef$. This decrease in current happens when the trajectory of n_g crosses the dashed lines in fig. 4, which are known as the backtunneling thresholds. A straightforward calculation shows that this threshold (black dashed line in fig. 4) is

$$n_g^b = \frac{eV_b + \Delta}{2E_c} + \frac{1}{2} \tag{26}$$

As we cross this threshold, it becomes possible for an electron to tunnel back from the island through the left junction, bringing the charge state back to 0 from 1, resulting in no net charge transfer for that particular cycle and thus a decreased current. While errors caused by backtunneling are decreased as we increase the bias voltage, increasing the bias results in extra electrons tunneling on the island, which increase the current output of the device as shown in fig. 7. Therefore, choosing the bias voltage requires balancing between these two thermal error mechanisms. The relative error rate caused by backtunneling scales as e^{-eV/k_BT} whereas the relative error rate caused by extra tunneling events scales as $e^{-(2\Delta - eV)/k_BT}$ [18]. The total error rate is minimized when $eV_b \simeq \Delta/2$ per junction.

At even higher amplitudes, we notice that the current output increases to $3ef$. This happens when the trajectory extends to the regions where the charge states $n = 2$ and $n = -1$ are stable. For metrology, these plateaus are not relevant since backtunneling is unavoidable and the current output starts decreasing immediately after the onset of this current step. The larger current also heats the island more.

Fig. 8 shows simulated pumping curves at different values of the product $\Delta/(e^2 R_T f)$, where R_T is the resistance per junction. Therefore it displays how the performance of the turnstile is affected by the operating frequency as well as the tunneling resistance of

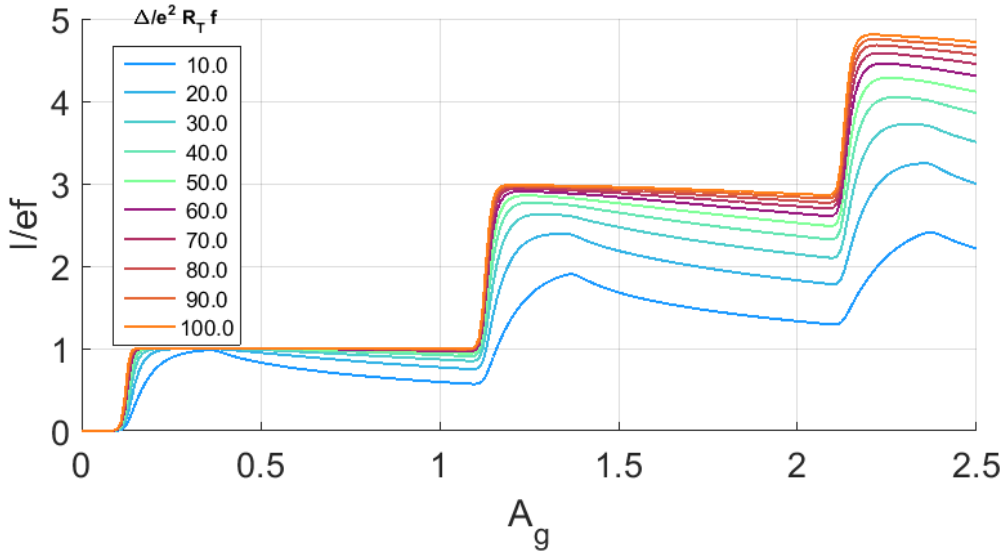

Figure 8: Simulated pumping curves for different frequencies at a constant bias voltage $eV_b = \Delta/2$ per junction.

the junctions. It can be seen that the performance degrades at higher frequencies and resistances. This is due to missed tunneling events: at higher frequencies the amount of time spent in the region where tunneling is possible is smaller and the electrons may not have enough time to tunnel through the junctions. This also explains why the current output increases until the backtunneling threshold. As the resistance increases, the single-electron tunneling rates are smaller according to equations (10) and (11).

From equations (25) and (26) we can calculate that the width of the region between the forward and backward tunneling thresholds is eV_b/E_c. This would suggest that the current step becomes wider as we decrease the charging energy. However, due to various higher-order processes, this is not the case. In an SINIS structure, the dominant higher-order processes are two-electron processes that do not break Cooper pairs. Such processes are the elastic co-tunneling and Andreev tunneling. Co-tunneling is effectively suppressed by the superconducting gap, which leaves Andreev tunneling as the dominant two-electron process. In Andreev tunneling, an electron coming from the superconductor is reflected as a hole or, in other words, two electrons tunneling from the normal metal tunnel and form a Cooper pair in the superconductor. Since the process involves transport of two electrons, it causes excess current [28].

The change in energy when two electrons are added or removed from the island is, according to equation (20)

$$\delta E^{\pm\pm} = \mp 4E_c(n - n_g \pm 1) \mp 2eV, \tag{27}$$

when taking into account the bias. Since the process does not involve breaking Cooper pairs, it remains allowed as long as the energy gain is positive. Therefore, we can easily

calculate the threshold for Andreev tunneling, which gives

$$n_g^A = n \pm (1 - \frac{eV_b}{\Delta}). \tag{28}$$

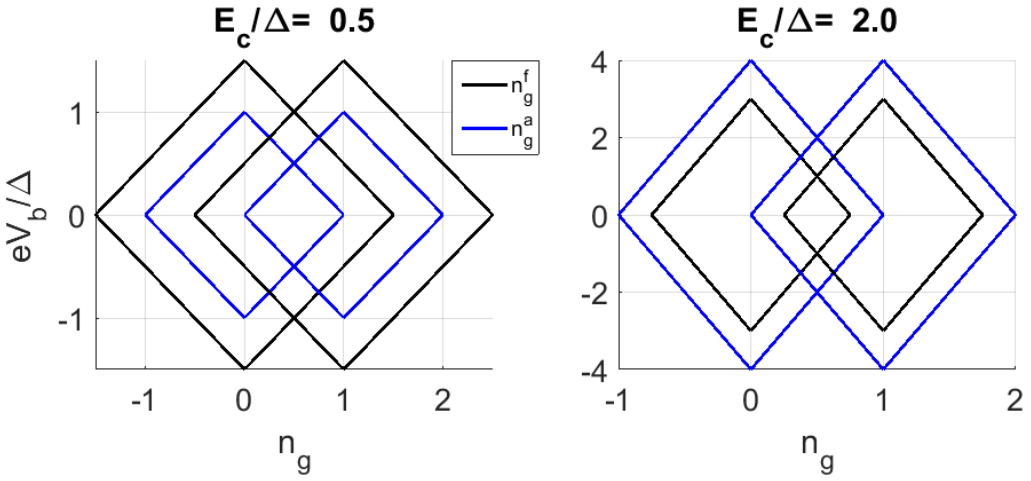

Figure 9: Thresholds for single-electron and Andreev tunneling for two different charging energies.

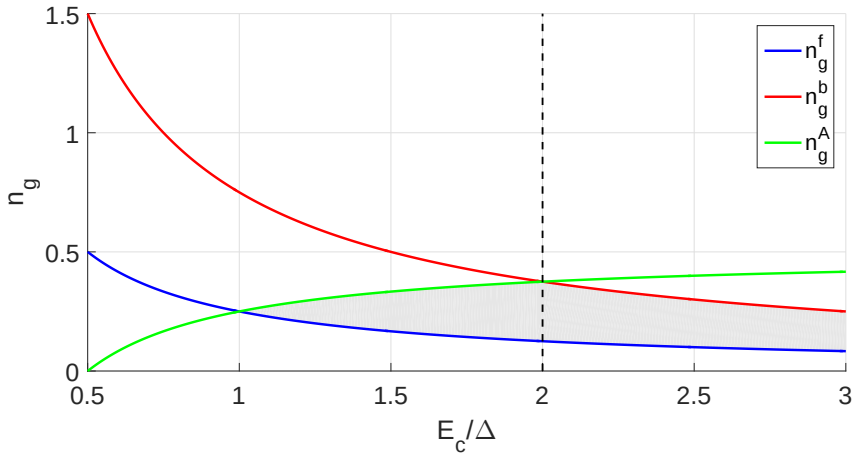

Figure 10: The forward (blue), backward (red) and Andreev (greem) tunneling thresholds as a function of charging energy. The shaded region corresponds to the values of the pumping amplitude, which yields a flat plateau since the backtunneling and Andreev tunneling are suppressed.

In fig. 9 we have plotted the thresholds for both Andreev tunneling and single-electron tunneling as a function of charging energy. It can be seen that at low charging energies, the

threshold for Andreev tunneling is lower than for single-electron tunneling, which means that a flat pumping plateau cannot be achieved in such case. In order for the plateau to exist in the first place, we must have $n_g^f > n_g^A$. When the correspoding thresholds are plugged into the inequality, we obtain $E_c/\Delta > 1$, meaning that the charging energy should be at least higher than the superconducting gap.

In order to have the plateau as wide as possible, we need to maximise $\min(n_g^b, n_g^A)$. In fig. 10 we have plotted the three tunneling thresholds at $eV_b = \Delta$ as a function of the charging energy. From the plot we can see that the plateau is widest when $E_c = 2\Delta$.

3.5 Quasiparticle excitations

As shown earlier, the Hamiltonian describing the electrons in the superconductor can be diagonalized by introducing the operators $\gamma^\dagger$ and γ, which are linear combinations of the standard electronic creation and annihilation operators. Therefore we refer to excitations in superconductors as quasiparticles. The number of these excitations decays exponentially as we decrease the temperature.

Deriving the density of states for the superconductor revealed that the density of states has two branches. In the ground state, electrons occupy the states lying below the energy gap whereas the high-energy branch remains vacant. As electrons are excited, states lying above the energy gap become occupied, leaving vacancies on the low-energy branch. The former are called particle like excitations whereas the latter are hole like excitations. The total number of quasiparticles on both branches is equal.

The density of quasiparticles in the high-energy branch is

$$n_{qp}^{E>\Delta} = D(E_F) \int_\Delta^\infty dE n_S(E) f_S(E), \tag{29}$$

where $D(E_F)$ is the density of states at the Fermi energy in the normal state. In order to evaluate the integral, we assume that the temperature $k_B T \ll \Delta$. In this regime, the Fermi-Dirac distribution $\frac{1}{1+e^{E/k_BT}} \approx e^{-E/k_BT}$ for $E \geq \Delta$ and we have

$$n_{qp}^{E>\Delta} = D(E_F) \int_\Delta^\infty dE e^{-E/k_B T_S} \frac{E}{\sqrt{E^2 - \Delta^2}} = D(E_F)\Delta K_1(\Delta/k_B T_S). \tag{30}$$

Above, $K_1(x)$ is the modified Bessel function of the second kind. Since we assumed the temperature to be low, we can write $K_1(x) \approx \sqrt{\frac{\pi}{2x}} e^{-x}$ for $x \gg 1$, to obtain the total density of quasiparticles:

$$n_{qp} = 2n_{qp}^{E>\Delta} = D(E_F)\sqrt{2\pi k_B T_S \Delta} e^{-\Delta/k_B T_S}, \tag{31}$$

which gives the relation between the quasiparticle density and the temperature of the superconductor.

The effect of these thermally excited quasiparticles on the performance of the SINIS turnstile can be estimated by considering the tunneling rates in the subgap regime, when the energy gained in a tunneling event is less than the gap energy. If the temperature of

the normal metal is low, we have $1 - f_N(E + \delta E) \approx 1$ for $E > \Delta$ and $-\Delta < \delta E < \Delta$. We may then write the tunneling rates as

$$\Gamma^{sg}_{S\to N} = \frac{1}{e^2 R_T} \int_{\Delta}^{\infty} dE n_S(E) f_S(E). \tag{32}$$

By comparing this with equation (29) we see that

$$\Gamma^{sg}_{S\to N} = \frac{n_{qp}}{2e^2 R_T D(E_F)}, \tag{33}$$

and the excess current becomes simply $I = n_{qp}/eR_T D(E_F)$. From a device design point of view, we notice that the errors caused by quasiparticle tunneling can be reduced by increasing the resistance of the sample, which leads to a trade-off: higher resistance leads to more missed tunneling events while lower resistance leads to excess currents due to quasiparticle excitations.

During turnstile operation, we remove electrons from one lead and inject them into the other. Since the electrons we remove lie below the gap and the electrons we inject in the other lead will be above the energy gap, this leads to so-called branch imbalance [31]. In this case, the validity of equation (31) is not evident. However, it has been shown that there is no significant branch imbalance during turnstile operations since the relaxation of the imbalance is fast compared to the quasiparticle injection rate [32]. We may thus use equation (31) with an elevated temperature in the superconducting leads. This also allows us to use the SINIS turnstile to probe the quasiparticle density.

In this work, we have used quasiparticle traps to reduce the number of quasiparticles. The trap is a piece of normal metal coupled to the superconducting leads either via a tunnel junction or a direct contact. As with the choice of other device parameters, such as the resistance, we have to balance between two properties: if the trap is too far away from the junction, the transport of the quasiparticles to the trap is not efficient. On the other hand, if the trap is too close and also in very good contact with the lead, it will deteorirate the superconductivity of the leads via inverse proximity effect [33], leading to a large value of the Dynes parameter γ in equation (14).

3.6 Heat transport in the superconducting leads

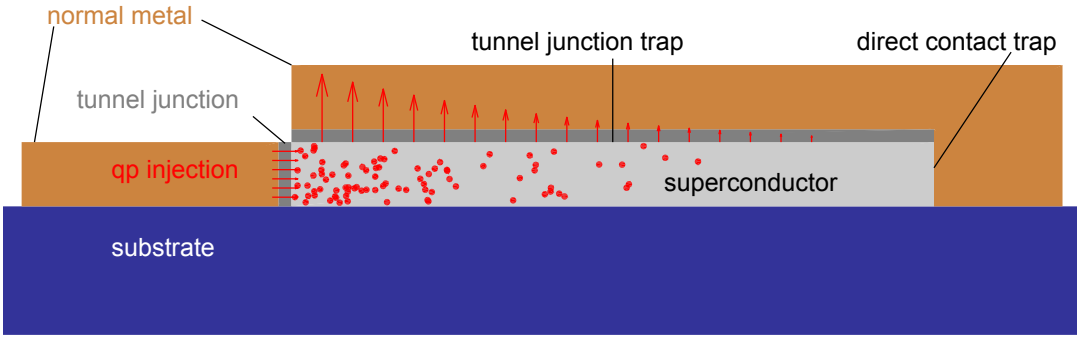

Figure 11: A schematic figure of the quasiparticle relaxation. The quasiparticles are injected to the superconducting lead via the tunnel junction connecting the lead to the normal metal island on the left. Quasiparticles are removed from the superconductor by a normal metal trap, which is coupled to the superconductor with a tunnel junction and a direct contact further away from the junction.

We model the transport of quasiparticles in the superconducting leads with a simple heat diffusion equation

$$\nabla \cdot \vec{J} = -p, \tag{34}$$

where $\vec{J}$ is the heat flux and p is the power removed per unit volume. We use Fourier's law $\vec{J} = -\kappa_S \nabla T$, where κ_S is the thermal conductivity of the superconductor. We will first compute the derivatives to obtain

$$-p = \nabla \cdot \vec{J} = -(\nabla \kappa_S) \cdot (\nabla T) - \kappa_S \nabla^2 T. \tag{35}$$

The thermal conductivity is given by [34]

$$\kappa_S = \kappa_N \frac{2F_1(-y) + 2y \ln\left(1 + e^{-y}\right) + y^2(1 + e^y)}{2F_1(0)}. \tag{36}$$

Above, κ_N is the thermal conductivity in the normal state, $y = \Delta / k_B T$ and

$$F_1(-y) = \int_0^\infty dx \frac{x}{1 + e^{x+y}}. \tag{37}$$

In the limit $k_B T \ll \Delta$ the thermal conductivity becomes

$$\kappa_S = \frac{6}{\pi^2} \left(\frac{\Delta}{k_B T} \right)^2 e^{-\Delta / k_B T} L_0 T / \rho_n \tag{38}$$

where $L_0 = (\pi k_B)^2 / 3e^2$ is the Lorentz number and ρ_n is the resistivity of the leads in normal state.

For simplicity, we only consider the strong exponential temperature dependencies for the heat conductivity. With this approximation, we may write the gradient of the thermal conductivity as

$$\nabla\kappa_S = \frac{2\Delta^3}{e^2\rho_N k_B T} e^{-\Delta/k_B T}\frac{\nabla T}{T^2}. \tag{39}$$

Substituting this into equation (35) yields

$$p = \frac{2\Delta^2}{e^2\rho_n T} e^{-\Delta/k_B T}\left[\frac{\Delta(\nabla T)^2}{k_B T^2} + \nabla^2 T\right] \tag{40}$$

We will now write equation (40) in terms of the quasiparticle density using equation (31). We will again consider only the strong exponential dependencies. Thus, the gradient of the quasiparticle density is

$$\nabla n_{qp} = \frac{D(E_F)e^{-\Delta/k_B T}\Delta\sqrt{2\pi k_B T\Delta}}{k_B T^2}\nabla T, \tag{41}$$

and the Laplacian

$$\nabla^2 n_{qp} = \nabla\cdot\nabla n_{qp} = \frac{D(E_F)\Delta\sqrt{2\pi k_B T\Delta}}{k_B T^2} e^{-\Delta/k_B T}\left[\frac{\Delta(\nabla T)^2}{k_B T^2} + \nabla^2 T\right]. \tag{42}$$

Comparing equations (40) and (42) we see that

$$p = \frac{\sqrt{2k_B T\Delta}}{\sqrt{\pi}e^2\rho_n D(E_F)}\nabla^2 n_{qp} \equiv D\nabla^2 n_{qp}, \tag{43}$$

where we have defined the diffusion constant $D = \frac{\sqrt{2k_B T\Delta}}{\sqrt{\pi}e^2\rho_n D(E_F)}$.

In order to study the transport in more detail, we need to derive an expression for the LHS of equation (43). Heat is removed from the leads by quasiparticles tunneling to the normal metal trap through an oxide layer. Since the leads and the normal metal trap are large we do not need to consider charging effects. Furthermore, the lead and the trap have the same potential. Therefore, we may use equation (13) with $\delta E = 0$ to obtain the power removed per unit volume

$$p_{trap} = \frac{2\sigma_T}{e^2 d}\int_\Delta^\infty dE E n_S(E)(f_S(E) - f_N(E)), \tag{44}$$

where σ_T is the conductance per unit area of the trap and d is the thickness of the superconducting leads. Evaluating the integral gives

$$p_{trap} = \frac{2\sigma_T\Delta^2}{e^2 d}(K_2(\Delta/k_B T_S) - K_2(\Delta/k_B T_N)). \tag{45}$$

In the low-temperature limit $\Delta/k_B T \gg 1$ we can approximate $K_2(\Delta/k_B T) \approx K_1(\Delta/k_B T)$ and we may use equation (30) to get

$$p_{trap} \approx \frac{\sigma_T\Delta}{e^2 d D(E_F)}(n_{qp} - n_{qp0}), \tag{46}$$

where n_{qp0} is the quasiparticle density of a fully thermalised superconductor. Substituting equation (46) into equation (43) finally gives

$$\nabla^2 n_{qp} = \lambda^2 (n_{qp} - n_{qp0}), \tag{47}$$

where $\lambda^2 = \frac{\sqrt{\pi\Delta}\rho_n\sigma_T}{\sqrt{2k_B T}d}$. This parameter characterises the distance the quasiparticles travel before relaxing to the temperature of the normal metal trap. Since n_{qp0} may be considered constant, we define $\tilde{n} = n_{qp} - n_{qp0}$ and write

$$\nabla^2 n_{qp} = \nabla^2 \tilde{n} = \lambda^2 \tilde{n}. \tag{48}$$

In order solve equation (48) for our lead geometries, we need to derive the necessary boundary conditions. We assume that the there is a direct contact to a normal metal trap that is at distance R from the junction. The direct contact forces the temperature of the leads to be the same as that of the normal metal, i.e.

$$\tilde{n}(R) = 0. \tag{49}$$

A second boundary condition comes from the quasiparticle injection: the total heating power at the junction must correspond to the injected power, which leads to the following boundary condition:

$$\int_{A_{inj}} d\vec{S} \cdot \vec{J} = P_{inj}, \tag{50}$$

where A_{inj} is the quasiparticle injection area. In a pumping experiment we may set $P_{inj} = f\Delta$, which allows us to estimate the quasiparticle density also as a function of pumping frequency. Using Fourier's law and equation (41) we can write the boundary condition as

$$-\frac{\sqrt{2k_B T\Delta}}{\sqrt{\pi}D(E_F)\rho_n e^2}\int_{A_{inj}} dS(\hat{n}\cdot\nabla n) = -D\int_{A_{inj}} dS(\hat{n}\cdot\nabla n) = P_{inj} \tag{51}$$

We will now study the effects of the lead geometry on the quasiparticle density, particularly near the tunnel junction. We first consider diffusion in a wire that has length L, width w and thickness d. If $L \gg w, d$ we may consider the diffusion in only one dimension and obtain a general solution

$$\tilde{n}(x) = Ae^{\lambda x} + Be^{-\lambda x}. \tag{52}$$

Applying the first boundary condition gives

$$\tilde{n}(x) = B(e^{-\lambda x} - e^{\lambda(x-2L)}) \tag{53}$$

We assume that quasiparticles are injected through the other end so that the normal vector at the junction is parallel to the x-axis. Then equation (51) becomes $-wdD\frac{\partial\tilde{n}}{\partial x}\big|_{x=0} = P_{inj}$, which gives

$$\tilde{n} = \frac{P_{inj}e^{-\lambda L}}{2wdD\lambda\cosh(\lambda L)}(e^{-\lambda(x-2L)-e^{\lambda x}}). \tag{54}$$

From this, we can evaluate the quasiparticle density at the junction:

$$\tilde{n}(0) = \frac{P_{inj} \tanh(\lambda L)}{wdD\lambda}. \tag{55}$$

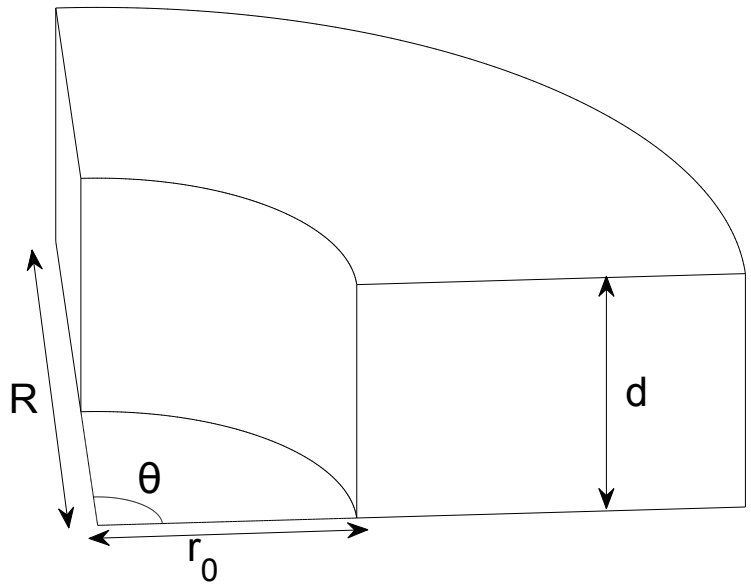

Figure 12: The geometry used to solve equation (48) in polar coordinates. The quasiparticles are injected at distance r_0 and the direct contact trap is located at distance R. The thickness of the lead is d.

The experiments presented in this thesis were performed with leads that have the shape of a circular sector. In this case we may write equation (48) in polar coordinates. Assuming there is no azimuthal dependence we get

$$r^2\tilde{n}''(r) + r\tilde{n}'(r) - r^2\lambda^2\tilde{n}(r) = 0. \tag{56}$$

By making a change of variable to $x = \lambda r$ we notice that equation (56) is a modified Bessel differential equation and we get a general solution

$$\tilde{n} = AI_0(\lambda r) + BK_0(\lambda r), \tag{57}$$

where I_0 and K_0 are modified Bessel functions of first and second kind, respectively. Assuming the lead to terminate to the direct contact trap at distance R away from the junction, we get

$$\tilde{n}(r) = B\left[K_0(\lambda r) - \frac{K_0(\lambda R)}{I_0(\lambda R)} I_0(\lambda r)\right]. \tag{58}$$

We assume that the quasiparticles are injected radially at distance r_0 from the tip of the leads through a cylinder surface with height d, and radius r_0. Assuming the leads open

at a fixed angle θ, we get $A_{inj} = \theta r_0 d$ and $\hat{n} \cdot \nabla \tilde{n} = \frac{\partial \tilde{n}}{\partial r}$ so the second boundary condition reads $-D\theta r_0 d \frac{\partial \tilde{n}}{\partial r}\big|_{x=0} = P_{inj}$ and the quasiparticle density becomes

$$\tilde{n}(r) = \frac{P_{inj}[I_0(\lambda R)K_0(\lambda r) - K_0(\lambda R)I_0(\lambda r)]}{\lambda D\theta r_0 d[K_1(\lambda r_0)I_0(\lambda R) + K_0(\lambda R)I_1(\lambda r_0)]} \tag{59}$$

and the quasiparticle density at the junction becomes approximately

$$\tilde{n}(r_0) \approx \frac{P_{inj}K_0(\lambda r_0)}{\lambda D\theta r_0 d K_1(\lambda r_0)}. \tag{60}$$

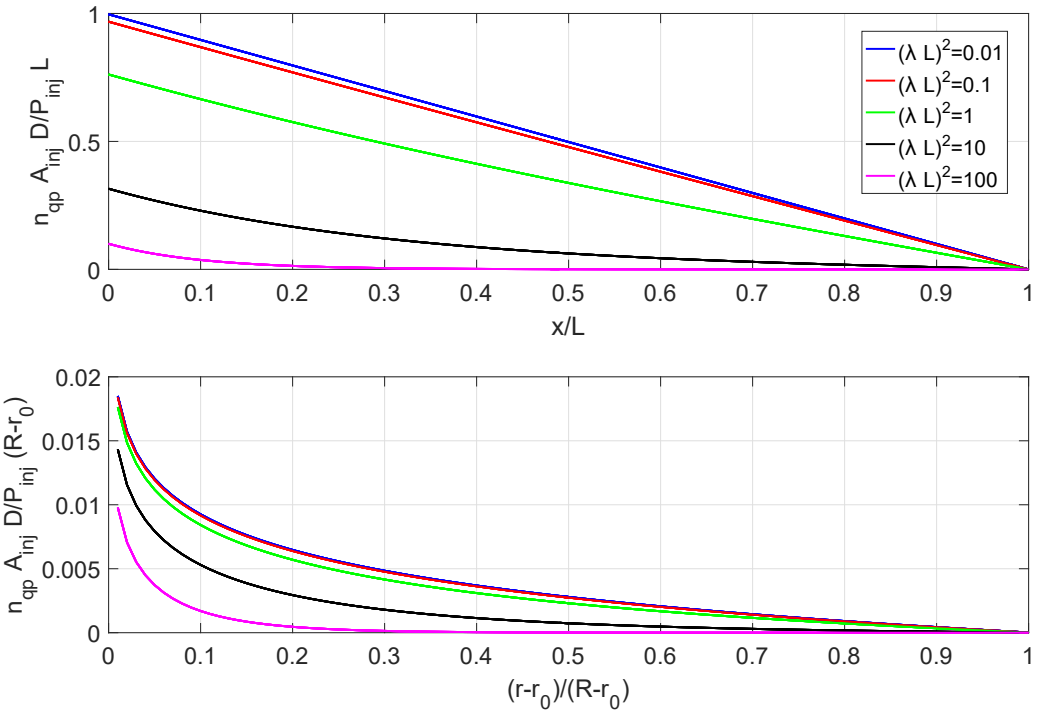

Figure 13: The quasiparticle density as a function of distance from the junction for the wire (upper panel) and the sector shaped leads (lower panel) at five different transparancies of the oxide trap. We have normalised the distance by the length of the lead. In the lower panel, the length is defined as $R - r_0$, where r_0 and R are defined in fig. 12.

In fig. 13 we have plotted the quasiparticle density in the leads for various transparencies of the oxide trap. We can clearly see that using the widening leads, one achieves a much lower quasiparticle density. This is due to the quasiparticles spreading over a larger area.

It should be noted that the simple form of boundary condition (51) can only be used if the leads and the island have similar thicknesses. If the leads are much thicker than

the island, several points need to be considered: first of all, having thicker leads increases the effective opacity of the trap, which increases the overall quasiparticle density. On the other hand, we noticed simply by considering the wire and sector-shaped leads that the quasparticle relaxation is more efficient for the latter geometry. This is due to the heat flow spreading over a larger area. If the leads are very thick, we can no longer assume that the diffusion occurs on a two-dimensional plane. The simplest 3D model would be to solve equation (48) in spherical coordinates. The shape of the leads result in rather complex boundary conditions so we will instead consider a situation where the quasiparticles relax only via the direct contact trap, i.e. we set p_{trap} to zero. We also omit the angular dependence but since the dimensions of our structures are much larger than the length scale set by $\sqrt{A_{inj}} \sim r_0$, this approximation is valid at least in the vicinity of the junction.

We obtain the following solutions:

$$\tilde{n} = \frac{P_{inj}}{A_{inj}D}(L - x) \text{ (wire)} \tag{61}$$

$$\tilde{n} = -\frac{r_0 P_{inj}}{A_{inj}D} \ln \frac{R}{r} \text{ (polar)} \tag{62}$$

$$\tilde{n} = \frac{r_0^2 P_{inj}}{A_{inj}D}(\frac{1}{r} - \frac{1}{R}) \text{ (spherical)} \tag{63}$$

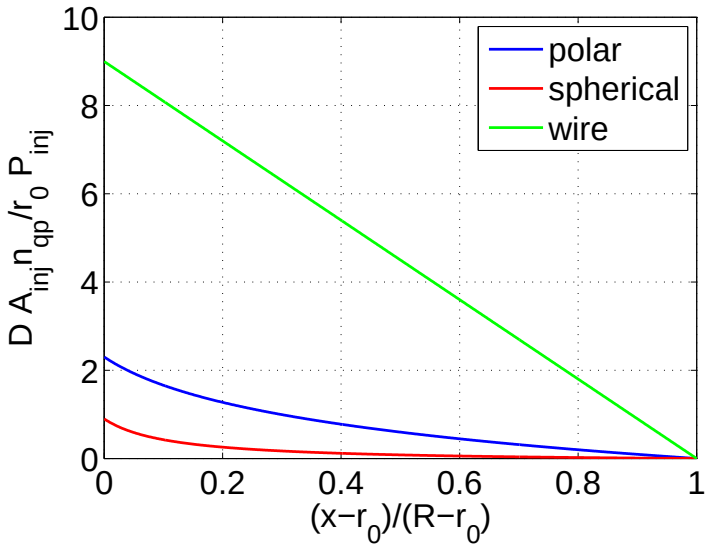

Figure 14: The quasiparticle densities in the absence of an oxide trap for three different geometries. We have used $R/r_0 = 10$.

In fig. 14 we have plotted the quasiparticle density as a function of distance from the junction. We clearly see that in the spherical geometry, the quasiparticle density is the

smallest, which we attribute to the more efficient spreading of the heat flow. Therefore we may conclude that despite the possibly reduced tunneling into the trap, spreading the heat flow over an even larger area may result in an overall reduction in the quasiparticle density for thicker leads.

4 Experimental methods

4.1 Sample fabrication

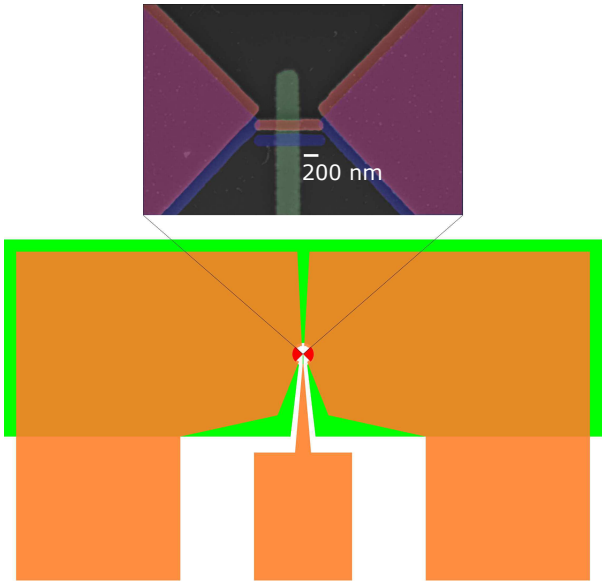

Figure 15: A schematic of the entire sample design with a zoomed-in false color SEM image of the turnstile. In the schematic design, the green part is the ground plane and the orange parts are the bonding pads, which also act as a direct contact quasiparticle trap. In the false color image, the red parts are copper and the blue parts are aluminum. Note that the gate electrode bonding pad was deposited together with the ground plane, but it is shown here in orange for clarity.

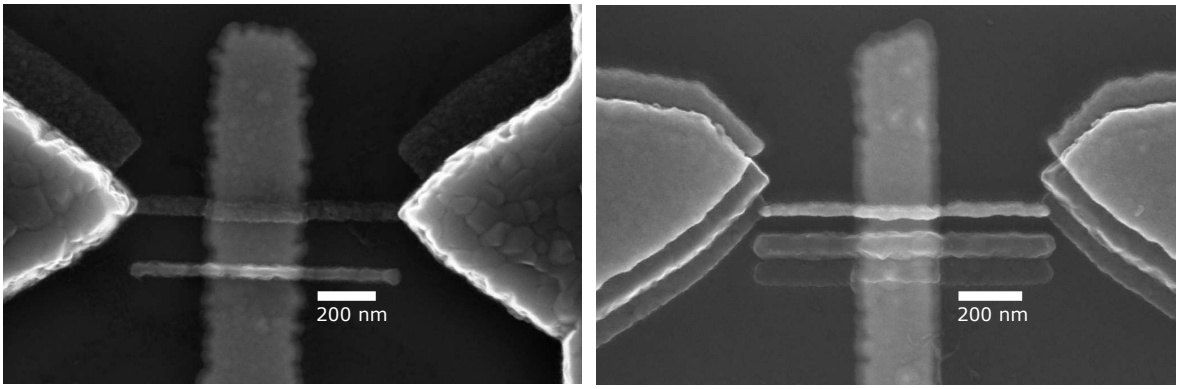

Figure 16: Scanning electron micrographs of the samples with thick superconducting leads. On the left is a sample with an AlMn island. The bright, downwards-shifted shadow copy of the structures is the undoped aluminum while the darker areas are AlMn. The sample on the right was fabricated using the three-angle technique. The metals in the middle and bottom are aluminum whereas the metal on the top is copper.

The devices studied in this thesis were fabricated on thermally oxidised silicon wafers using the shadow evaporation technique [35]. In this technique, we use a mask suspended on top of a copolymer layer and deposit the structures at two different incident angles. After evaporating the first metal, we may fill the deposition chamber with oxygen to grow an insulating oxide layer followed by deposition of the second metal. With proper mask design, tunnel junctions are formed where the metals overlap, as shown in fig. 17. Scanning electron micrographs of typical samples are shown in figs. 15 and 16.

We first fabricated ground planes and the RF gates underneath the turnstiles, as well as alignment markers for subsequent lithography steps. The ground plane is simply a large piece of conductor underneath the turnstiles. The main purpose of the ground plane is to reduce the effect of environmentally activated tunneling [36]. The ground plane was fabricated by first spin-coating the wafers with a single, approximately 300 nm thick layer of AR-P 6200 e-beam resist [37]. The resist was then patterned with electron beam lithography (EBL). In EBL, we focus an electron beam on specific parts of the resist. This breaks down the long polymer chains of the resist, making them soluble to a suitable developer.

After patterning and developing the wafer, we deposited the ground planes and gates. The deposition was done using electron beam physical vapor deposition (EBPVD). In this process, we heat a piece of the target metal with an electron beam, causing it to melt and then evaporate. In high vacuum, the metal atoms take a line-of-sight passage to the substrate, forming a thin film. The evaporation rate was monitored using a quartz crystal microbalance. The ground planes and the gate consist of a 30 nm thick gold layer sandwiched between two 2 nm thick layers of titanium. The titatium layer underneath the gold facilitates the adhesion of the gold layer whereas the layer on the top layer helps the growth of the dielectric aluminum oxide layer in a subsequent step of the process.

After depositing the films, we remove any remaining resist as well as the metal residing on top of the resist layer in the so-called lift-off step. This consists of immersing the wafer in a suitable chemical for several hours. For our samples, we used Allresist AR 600-546. [37]

Next, we isolated the ground planes and gates by growing a layer of aluminum oxide using atomic layer deposition (ALD) [38].

Following the ALD, we performed another lithography, where we fabricated the bonding pads and the normal metal leads extending roughly 10 μm away from the turnstile junctions. These are displayed in orange in fig. 15. The process was essentially the same as the previous lithography step with the only difference being that the bonding pads were made out of gold palladium to prevent them from oxidising, and the thin titanium layer on top was omitted. Preventing oxidation is crucial since we want the contact between the superconducting leads and the normal metal leads extending from the bonding pads to be clean. This is because these normal metal leads act as the direct contact trap discussed in the previous section.

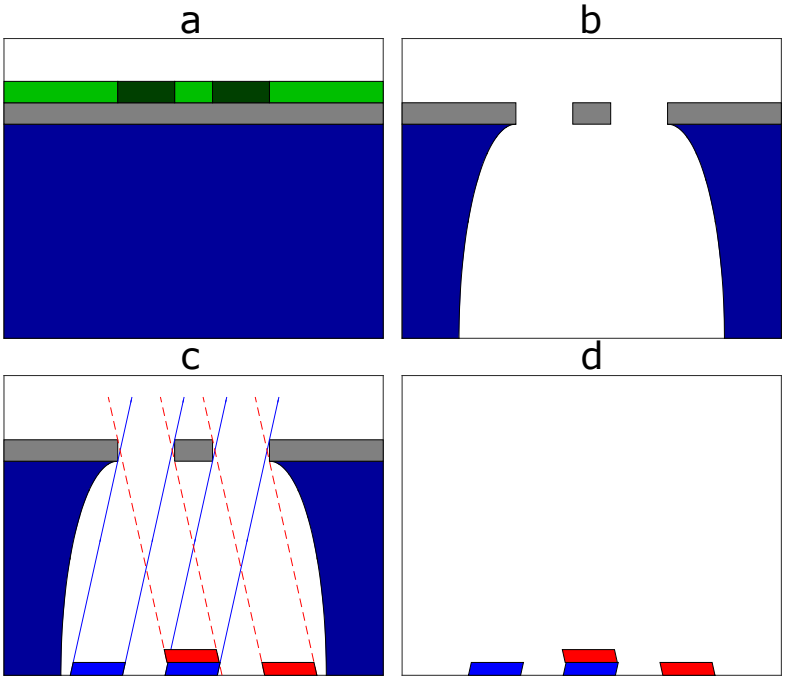

Figure 17: A schematic figure of the shadow evaporation technique. The lithography is done using a stack of three materials on the substrate. On the bottom is a thick layer of a copolymer (blue). In this work, the copolymer used was poly-methyl metacrylate (P(MAA-MMA)). On top of the copolymer is a thin film of germanium (grey). On top of the germanium we spin-coat a thin layer of PMMA (green), which is patterned using a focused electron beam (a). The pattern is transferred on the germanium using reactive ion etching. We also form an undercut in the copolymer layer underneath the germanium (b). Metal is deposited through the germanium mask at two different angles (c) and tunnel junctions are formed where the metals overlap. Finally the germanium, the copolymer and any metal deposited on top of the mask is removed in the lift-off step (d). The germanium layer was only used for the turnstiles. When fabricating the RF gate, the ground plane and the bonding pads, we only need a single resist layer since we do not perform a multi-angle evaporation. Note that the thicknesses of the layers are not to scale.

The third lithography step differed from the two previous steps in several ways. This is mainly because the turnstiles were fabricated using the shadow evaporation technique, which is sketched in fig. 17. We first spin-coat a layer of the copolymer. This copolymer layer needs to be sufficiently thick so that we can deposit the small structures at small incident angle in order to prevent the mask from blocking. A single P(MMA-MAA) layer is 400-500 nm thick, which is sufficient. After spinning the copolymer layer, we perform a soft bake step to remove any excess solvent.

After coating the wafer with the copolymer, we evaporate a 22 nm thick germanium film on top of the copolymer layer. We then spin-coated the wafer with PMMA, which

was then patterned using EBL. After patterning the resist, part of the wafer is cut into smaller chips, which are processed further individually.

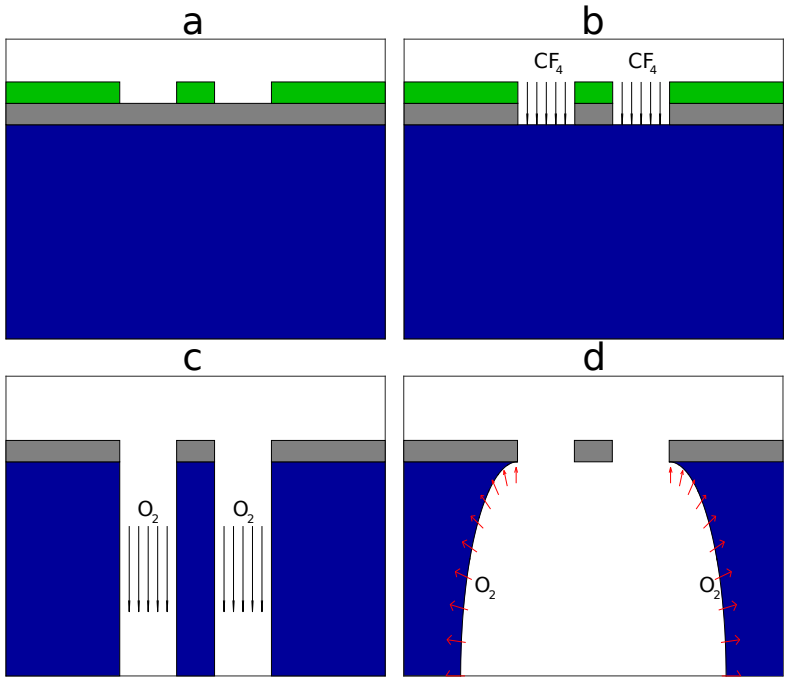

Figure 18: The Ge mask development process. The resist parts that were exposed in the EBL are removed by immersing the chips in a solution containing MIBK and IPA (a). The pattern is then transferred into the germanium by etching the chip with CF_4 plasma (b). Finally, the undercut is formed in two steps: first by exposing the chips to a low-pressure oxygen plasma to etch the copolymer somewhat anisotropically (c), followed by an isotropic etching step with higher pressure (d). The oxygen plasma also removes the PMMA layer on top of the germanium.

In order to transfer the patterns from the PMMA into the germanium film, we used a combination of wet etching and reactive ion etching (RIE). This development process is sketched in fig. 18. We first immersed the chips in a mixture of 1:3 volumetric ratio of methyl isobutyl ketone (MIBK) and isopropyl alcohol (IPA), followed by rinsing the chips in pure IPA and blow-drying them with nitrogen. In this step, the development time is rather crucial since if the chips are kept in the mixture for too long, the features become more round whereas if the time is not long enough, all of the exposed PMMA might not be removed.

After the wet etching, we perform the RIE by first exposing the chips to a CF_4 plasma. This etches the germanium underneath the exposed parts of the PMMA, transferring the pattern on the germanium film. Finally, we create the undercut: we expose the chips to an oxygen plasma in the RIE tool, which etches the copolymer underneath the germanium film. The oxygen also removes the PMMA on top of the germanium.

After development, we deposit the structures using EBPVD. For the samples with thin leads, we first deposit an aluminum film with a thickness of around 25 nm. The aluminum layer defines the superconducting parts of the turnstiles. The deposition of the aluminum is followed by an immediate in-situ oxidation to form an AlO_x layer on top of the aluminum. The properties of the oxide layer can be tuned by changing the pressure and the oxidation time. This way we can control the tunneling resistances of the junctions. The oxide layer is typically a few nm thick. After oxidation, we deposit the copper parts at a different angle, as discussed earlier. A typical evaporation rate was 2-3 Å/s. The rate was measured using a quartz crystal microbalance. This copper layer acts as the normal metal for the turnstiles. The copper is deposited at a slightly tilted angle to shift the patterns so that the copper island overlaps with the aluminum leads. In this step, large areas of copper are also deposited on top of the superconducting leads. This forms the oxide traps. The copper layer was usually around 30 nm thick.

Finally, we perform the lift-off to remove the rest of the resist and only leave the metallic structures on the chips. This is done simply by immersing the chips in acetone. We then quickly rinse the chips in IPA and blow-dry them with nitrogen.

For the samples with the thick aluminum leads we tried two approaches. Since the aim is to fabricate aluminum leads that are an order of magnitude thicker than the normal metal parts, while keeping the charging energy high, the normal metal has to be deposited first. This poses a problem since fabricating the tunnel junctions relies on oxidising the superconducting aluminum. In this work, we investigated two different approaches to overcome this challenge.

The first approach was a three-angle evaporation in which we would first evaporate a thin layer of aluminum. We would then immediately, without an oxidation in between, tilt the sample to a different angle and deposit another aluminum film with a much higher thickness. We would then oxidise both aluminium layers simultaneously, followed by deposition of the normal metal at a third angle. The tunnel junctions of the turnstile would be formed where the normal metal island overlaps with the thin aluminum film. This idea makes designing the mask more challenging in order to avoid any unwanted overlapping between the different islands and leads.

We studied in more detail the second method, which is based on the use of manganese-doped aluminum as the normal metal. The manganese suppresses the superconductivity of aluminum [39], while retaining the possibility to oxidise it in the same manner as undoped aluminium. Junctions based on AlMn have previously been used in e.g. radiation detectors [40] and NIS coolers [41]. This allows us to fabricate tunnel barriers in the same manner as before. The evaporation process itself was very similiar to the case of the thinner leads: we first deposited the doped aluminum and oxidised it and then deposited the undoped aluminum. We performed another oxidation step after fabricating the leads in order to reduce the influence of possible aging effects on the devices. The thickness profile for the two types of samples is schematically shown in fig. 19.

SEM images of samples fabricated with both of these methods are shown in fig. 16.

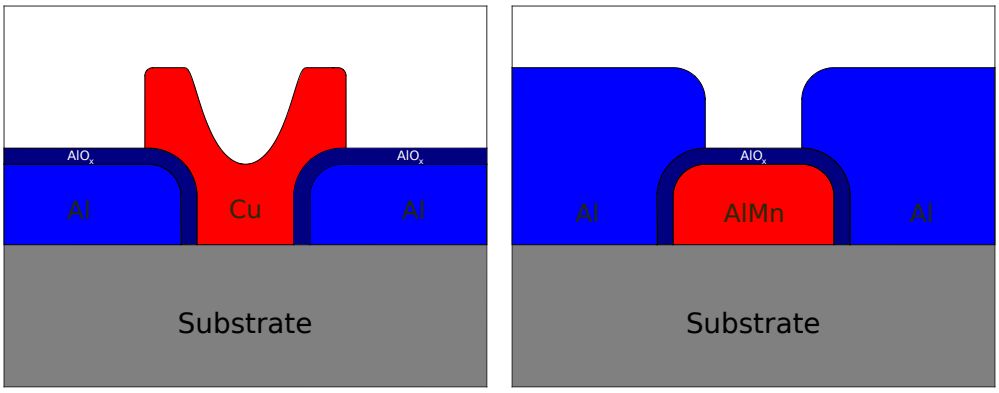

Figure 19: A schematic of the profiles of the samples with the thin (left) and thick (right) superconducting leads. For the thin leads, the superconductor (blue) is deposited first and then oxidised, forming the insulating layer. Finally, we deposit the normal metal (red). For the samples with the thick leads, we use manganese-doped aluminum as the normal metal. We first deposit the island and oxidise it before depositing the superconducting leads.

For the fabrication of the thicker leads, the angles used for evaporation were chosen differently compared to the case of thin leads. For the latter ones, we choose the angles symmetrically, i.e. we evaporate the normal metal parts at some angles $\pm\alpha$ with respect to the normal of the substrate surface, where α is determined by the resist thickness and the desired shift of the pattern. Due to this, the mask becomes partially blocked, which won't be a crucial issue if the films are sufficiently thin. For the thicker leads, this blocking will become more significant, which is why the thick films were evaporated at zero incidence angle.

4.2 Measurement setup

The samples were mounted on a custom made plastic dilution cryostat. The dilution cryostat is based on the enthalpy of mixing two isotopes of helium, namely ^{3}He and ^{4}He [42]. The base temperature of the cryostat we used was about 60 mK. The sample was mounted on the cryostat by attaching it to an In-shielded [43] sample stage with 6 dc and 2 RF lines. The bonding pads on the chips were connected to pads on the sample stage PCB by ultrasonic wedge bonding using Al wires with a diameter of 20 μm. The sample stage contained separate lines for the dc and RF signals. The dc lines were connected to a common 20 pin connector whereas each of the RF line had its own connector. The connectors and the bonding pads were joined by thermocoaxial cables with a length of some tens of centimeters. Thermocoaxial cables were chosen since they effectively filter out high-frequency noise due to skin effect [44]. Finally, the chip was covered with two nested caps with an indium seal on the inner cap, providing effective shielding from stray mirowave radiation from warmer parts of the cryostat. The sample stage was connected to the higher-temperature parts of the setup via a combination of thermocoax and twisted

pair cables.

A circuit diagram of the measurement setup is shown in fig. 20. We bias one of the leads using a Keysight 33522B waveform generator [45] at room temperature and a voltage divider. A typical voltage division used in the experiments was 1000, so that the voltages across the turnstile were of the order of hundreds of microvolts. The output current was amplified at room temperature with a Femto DDPCA-30 transimpedance amplifier [46]. The gains used ranged from 10^{10} to 10^{12}. The RF gate signal was generated with the same kind of waveform generator that was used for biasing the turnstile. The generator was connected to an attenuator, which was then connected to the gate on the device. The attenuators we used typically attenuate the signal by 40 dB at room temperature and by 20 dB at 4.2 K. The frequencies used typically ranged from 5 MHz to 30 MHz.

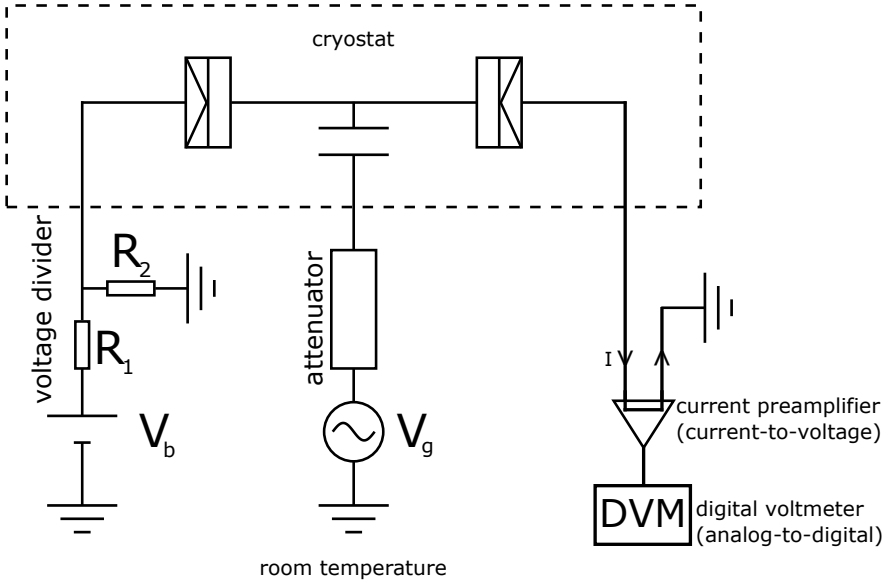

Figure 20: A circuit diagram of the measurement setup. We bias one of the leads of the turnstile using a voltage divider based on a simple network of resistors. The gate signal is fed through one of the RF lines in the cryostat. We read the output current through a dc line connected to the other lead. The dashed line shows which parts of the setup are at cryogenic cryogenic temperatures and which ones are at room temperature.

4.3 Measurement procedure

Before performing pumping experiments, we determined the dc characteristics of each sample, i.e. the superconducting gap, charging energy and tunneling resistance.

Majority of the detailed pumping experiments were performed in the gate open state, i.e. with $n_{g0} = 1/2$. To find the dc voltage corresponding to this gate offset, we exploit the periodicity of the current output by performing pumping at constant amplitude and sweeping over some gate voltage dc offset range. The pumping curves obtained this way

show flat plateaus whose midpoints correspond to the gate open position. The procedure is displayed in fig. 21. In order to determine the location of the midpoints, we fitted a double Gaussian function with the distance of the peaks corresponding to the dc gate period of the device, determined by the gate capacitance. This gate capacitance can be extracted from the dc measurements discussed earlier.

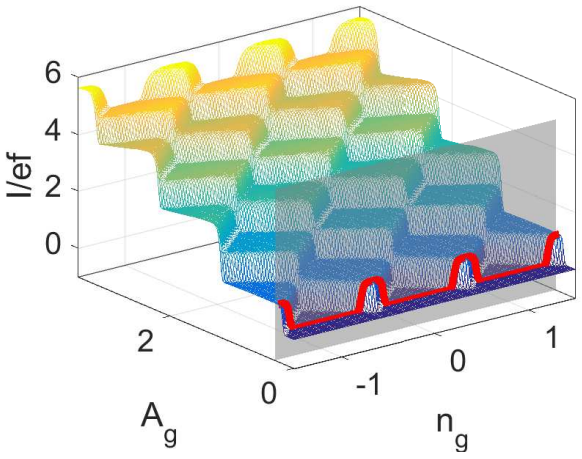

Figure 21: Finding the voltage offset corresponding to $n_{g0} = 1/2$. We measure the current output with a constant pumping amplitude A_g and varying gate offsets n_{g0}, which corresponds to determining the cross-section of the pumping surface and a plane corresponding to a constant offset (the grey plane). The obtained pumping current (red line) displays periodic plateaus or peaks whose midpoints correspond to $n_{g0} = 1/2$.

For each combination of bias and frequency, we performed several pumping measurements and average over all repetitions. Due to the asymmetrical biasing, the terms in equation (18) that contain the bias voltages do not cancel, resulting in a change in the dc offset as we change the bias voltage. In order to keep the driving signal around the degeneracy point, this change has to be compensated. Therefore for each bias voltage, we may either search the correct dc offset in the manner discussed above, or simply do it for several bias voltages and make a linear fit. There are three methods to get around this problem. The first one is searching for the correct gate offset in the manner discussed above for each bias. The second method relies on determining the junction capacitance appearing in equation (18) by determining the correct offset for several biases and making a linear fit. Finally, one could bias both leads and try to cancel the respective terms in equation (18). The latter two methods are susceptible to drifts in the equipment and are thus not as reliable as the first method.

We also determined the Dynes parameter for each of samples by measuring the dc characteristics in the subgap regime, i.e. $|V_b| < \Delta/e$ with $n_g = 1/2$ using an amplifier with a high gain. For these measurements, it is imperative that we are as close to the degeneracy point as possible. Because we can not say with certainty whether the turn-

stiles were at degeneracy for the duration of the entire subgap measurements, the Dynes parameters obtained this way are simply upper bounds.

4.4 Data processing

For both the dc measurements and pumping experiments, we solve equation (23) numerically and use equation (24) to evaluate the current expected from the theoretical model. For the dc measurements, we simulate the steady-state current for gate open and closed positions so that the current values obtained by sweeping the gate offset fall between the currents corresponding to these extrema. In the simulations we do not take into account the bias-dependent heating of the normal metal island, meaning that the true values of E_c are likely larger. The superconducting gap may be extracted from the width of the region where the current is suppressed in the gate open position whereas the charging energy is obtained from the width of the corresponding region in the gate closed position. The slope of the iv curve at large values of bias voltage gives the tunneling resistance.

The quasiparticle density can be estimated by determining the temperature of the superconducting leads and using equation (31). In order to determine the temperature, we make comparisons by solving the time-dependent master equation for each driving amplitude. We divide one period of the drive into time intervals of equal length. A more straightforward approach is then to simply start with a random probability distribution and calculate the tunneling matrix Γ for each time interval assuming that the tunneling rates do not change during said interval. We then use the tunneling rates to update the probability distribution and evaluate the current for each time instant using equation (24). We then average the output current over several periods of the drive in order to obtain the output current. We use the probability distribution at the end of the simulation as the initial guess for the simulation for the following amplitude.

Before comparing the experimental data to the simulations, we exclude any obvious erroneus measurements from the averaging. Most of these are caused by random jumps of the background offset charge. The superconductor quasiparticle temperature can be obtained by studying pumping experiments at constant frequency but different bias voltages. The frequency-dependence of the quasiparticle density and thus the temperature of the superconductor becomes evident by substituting $P_{inj} = \Delta f$ into equation (55) or (60). Due to the finite quasiparticle density, the current plateaux at different biases correspond to different currents, as seen in fig. 7, and at higher temperatures, they spread over a larger current range.

5 Results

Here we report measurements from three out of the several samples we investigated: one conventional sample with thin (30 nm) aluminum leads and a copper island and two structures with thick (350 nm) aluminum leads and an aluminum manganese island (35 nm). From here on, we refer to the thin-leaded sample as sample A and the thick-leaded samples as samples B and C. The opening angle of the leads in sample A was $\pi/2$ whereas the opening angle in samples B and C was π. Furthermore, samples B and C were both located on the same chip.

In this section we first present the results of the dc measurements on the samples, which allow us to extract values for the superconducting gap, charging energy and tunneling resistance. We will also present results from sub-gap leakage measurements, which allow us to extract a value for the Dynes parameter.

5.1 Dc characterisation of the samples

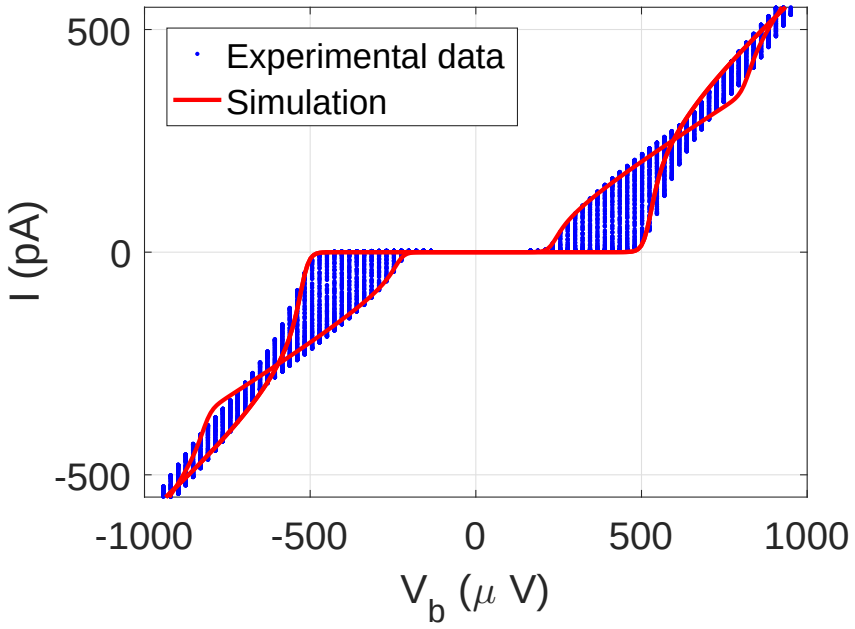

Figure 22: The dc current-voltage characteristics of sample A. The blue points are experimental data obtained by sweeping the gate offset at each bias voltage over multiple periods of gate modulation. The solid red lines are simulations corresponding to $n_{g0} = 0$ and $n_{g0} = 1/2$. From the data, we extract the parameters Δ=230 μeV, E_c=292 μeV and R_T=1.1 MΩ.

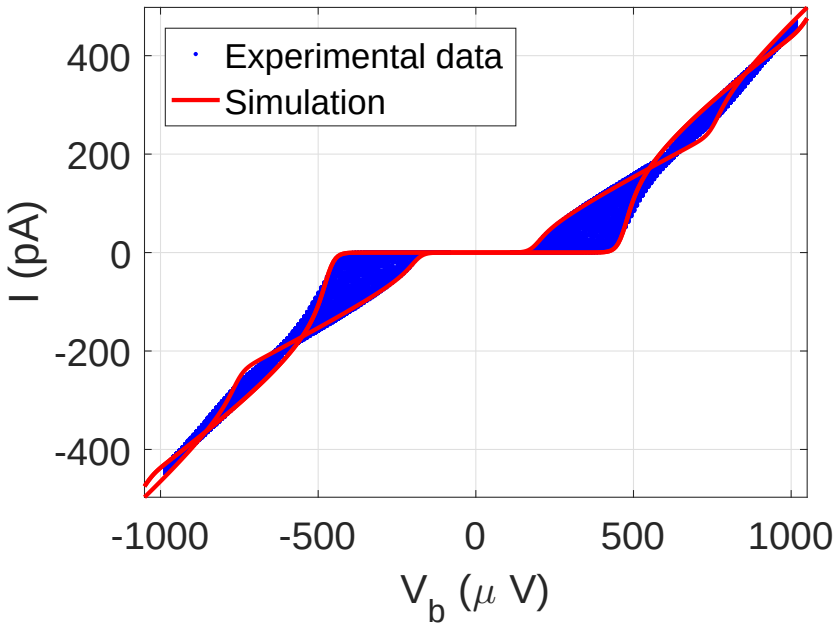

Figure 23: The dc current-voltage characteristics of sample B. We extract Δ=185 μeV, E_c=284 μeV and R_T=1.5 MΩ.

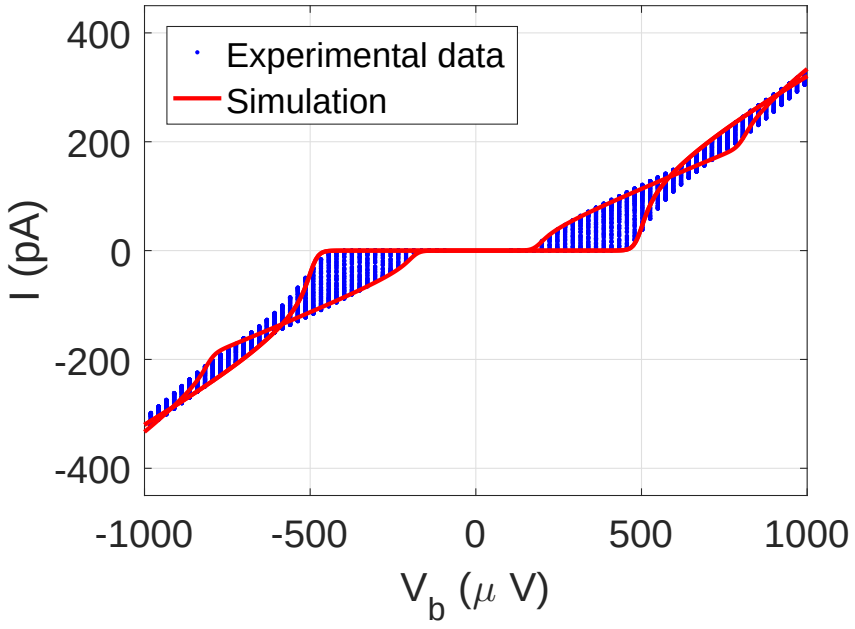

Figure 24: The dc current-voltage characteristics of sample C. We extract Δ=185 μeV, E_c=308 μeV and R_T=2.0 MΩ

In figures 22–24 we display the dc current-voltage characteristics of samples A, B and C, respectively. From the dc measurements as well as the leakage measurement presented in figures 25–27 we extract the following parameters:

Table 1: The characteristic dc parameters of the three measured samples

	Junction type	Δ (μeV)	E_c (μeV)	E_c/Δ	R_T (MΩ)	R_{sg} (GΩ)	γ
A	Al/Cu	230	292	1.27	1.1	180	5.9×10^{-6}
B	Al/AlMn	185	284	1.54	1.5	80	1.8×10^{-5}
C	Al/AlMn	185	308	1.67	2.0	110	1.4×10^{-5}

We may immediately see that for sample A the superconducting gap is larger than for the two other. This is expected since previous experiments [47] have shown that the superconducting gap for aluminum is larger for thin films. The value observed for samples B and C is relatively close to the bulk value of 170 μeV [48]. The resistances of all three samples are also relatively high, which limits the possible operation frequencies, as discussed earlier. However, by optimizing the oxidation conditions during sample fabrication, it is possible to fabricate junctions with significantly smaller resistances. Samples with lower tunneling resistances have already been measured since the measurements presented in this thesis.

The charging energies of all three samples are of similiar magnitude, which is to be expected since the design of the island is the same. Due to the smaller energy gap, the ratio E_c/Δ is higher for samples B and C, which is advantageous from the point of view of suppressing Andreev tunneling.

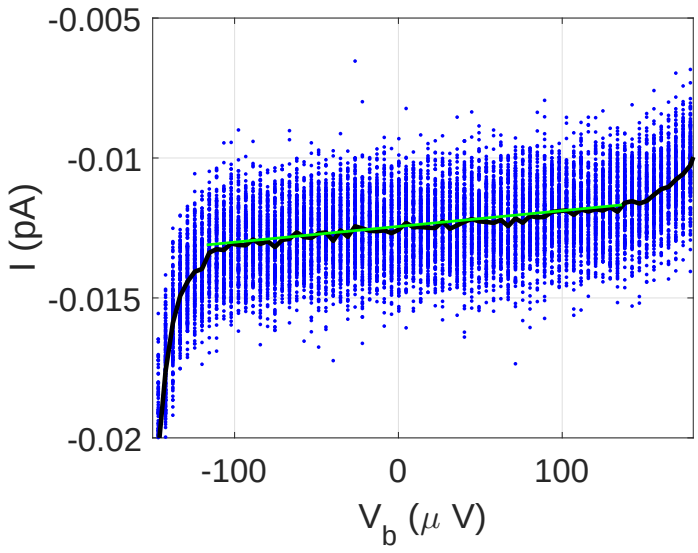

Figure 25: The sub-gap dc characteristics of sample A. The blue dots are the measured current values and the solid line is their average over 172 repetitions. The ratio of the subgap conductance, which is simply the slope of the green line, and large-V_b conductance (inverse of the tunneling resistance) gives the leakage parameter $\gamma \approx 5.9\times10^{-6}$.

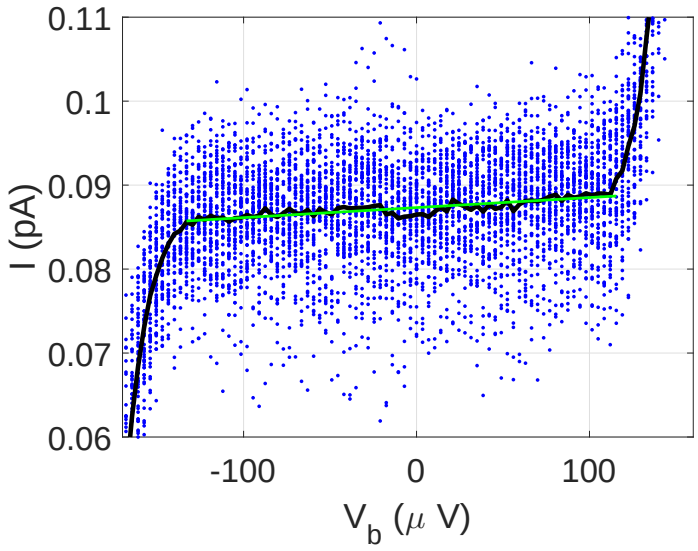

Figure 26: The sub-gap dc characteristics of sample B. For this sample, the measurement was repeated 58 times. From the slope of the green line, we obtain $\gamma \approx 1.8\times10^{-5}$.

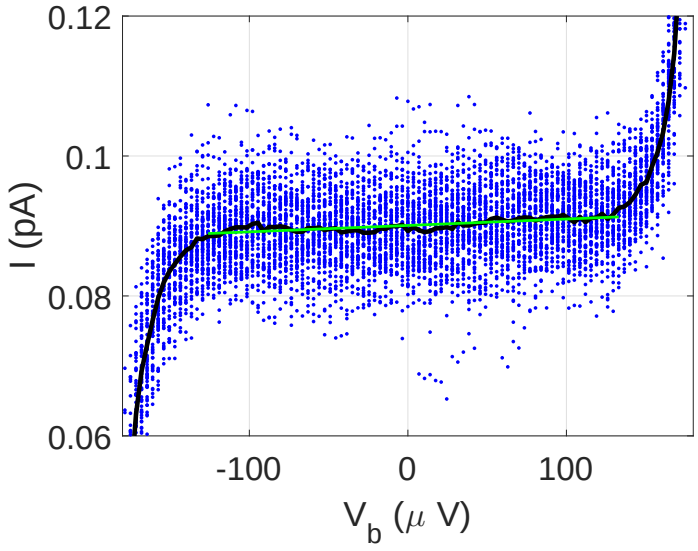

Figure 27: The sub-gap dc characteristics of sample C. For this sample, the measurement was repeated 66 times. We obtain $\gamma \approx 1.4\times10^{-5}$.

In figures 25–27 we have plotted the subgap IV characteristics of the three samples. The data was obtained by first determining the gate open position as described earlier for a single bias voltage and changing the gate voltage to compensate for the change in gate offset as we change the bias voltage.

From the slopes of the linear fits, we obtain $\gamma = 5.9\times10^{-6}$, $\gamma = 1.8\times10^{-5}$ and $\gamma = 1.4\times10^{-5}$ for samples A, B and C, respectively. However, these values can not be considered very reliable since the gate offset has to remain in the gate open position for the entire duration of the leakage measurement. If we do not perform the measurement at the degeneracy point, we obtain lower subgap conductance leading to smaller estimates for the leakage parameter.

5.2 Pumping results

In this subsection, we present the results of the pumping experiments on the three measured samples.

5.2.1 Sample A

For sample A, we show the results from pumping experiments at 10 MHz, 20 MHz, 30 MHz and 40 MHz sinusoidal drive, for several bias voltage around the optimum $V_b = \Delta/e$ per junction. For each combination of frequency and bias voltage, we averaged the experimental data over ten repetitions in this particular set of experiments.

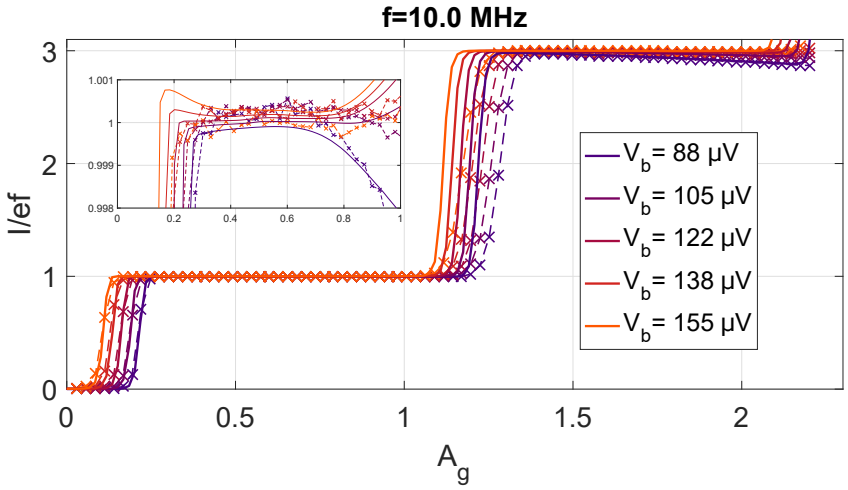

Figure 28: The measured pumping curves for sample A at 10 MHz. The crosses connected by the dashed lines are the experimental data. The solid lines are numerical simulations. The smaller panel displays the pumping plateaus on a zoomed scale.

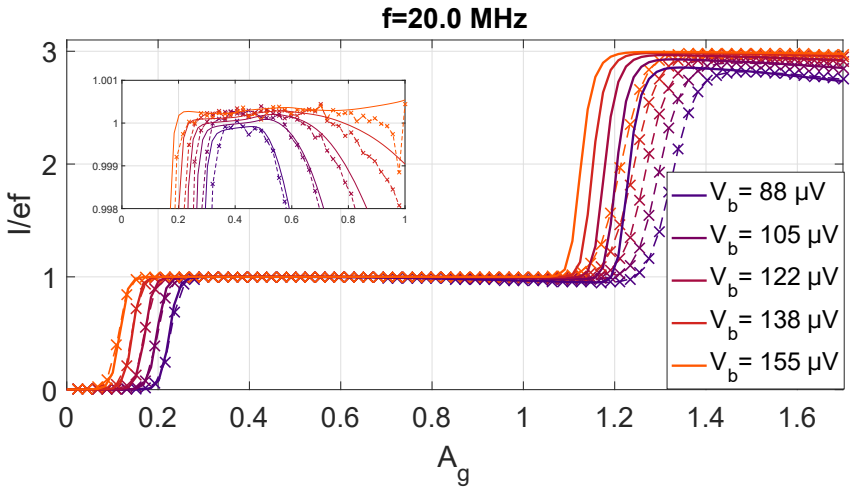

Figure 29: The measured pumping data for sample A at 20 MHz.

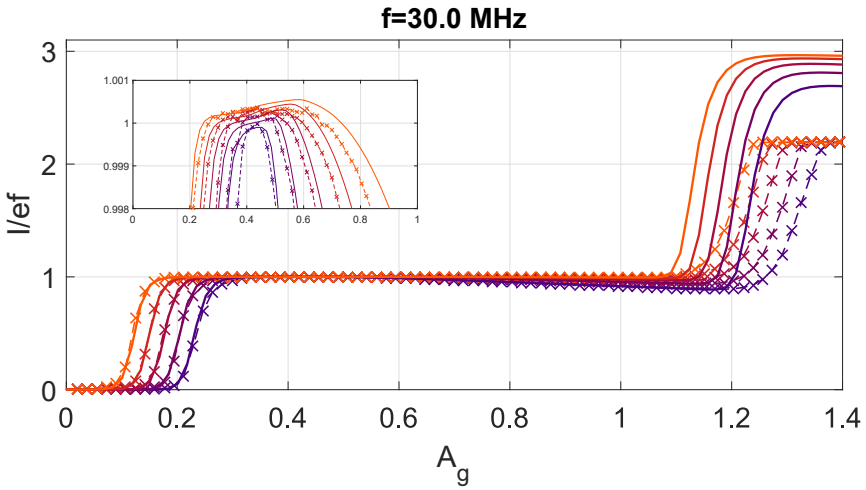

Figure 30: The measured pumping data for sample A at 30 MHz.

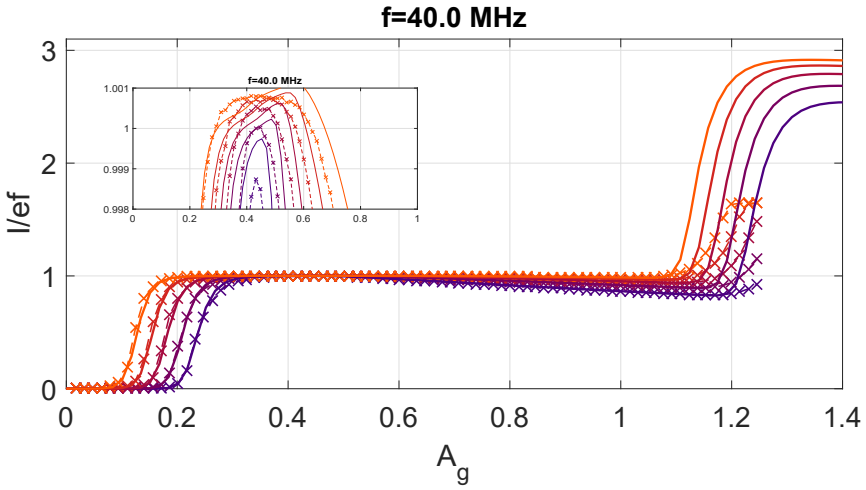

Figure 31: The measured pumping data for sample A at 40 MHz.

In figures 28–31 we show the measured pumping curves as well as numerical simulations. We are able to numerically reproduce the pumping results quite accurately on a large scale. However, the fits start to deviate significantly on the onset of the second pumping plateau. This may be due to drifts in the measurement equipment but also because at higher currents the turnstiles heat up more whereas we have only used a single, constant temperature for the N island in the simulations. However, this is not a crucial issue since we are only interested in the first pumping plateau. It can be clearly seen that the relative error is larger at low frequencies. This is to be expected since the current output is also smaller, which means that similiar absolute errors lead to higher relative errors. At higher frequencies, the second current plateau also seems to correspond to a lower current but this phenomenom is caused simply by the saturation of the current amplifier. Finally, the maximum pumping amplitude is lower at higher frequencies. The amplitude of the signal generated at room temperature was the same for all frequencies but the high-frequency signals get attenuated more in the RF lines of the cryostat and in particular the sample stage.

5.2.2 Samples B and C

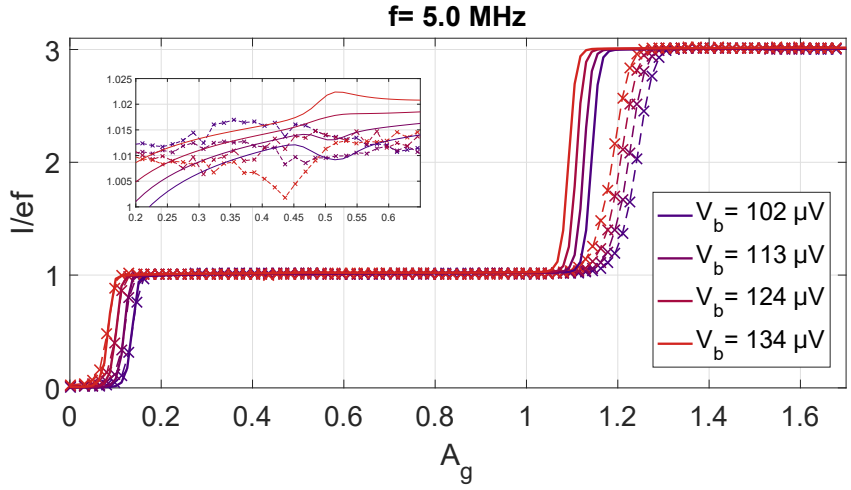

Figure 32: The measured pumping data for sample B at 5 MHz.

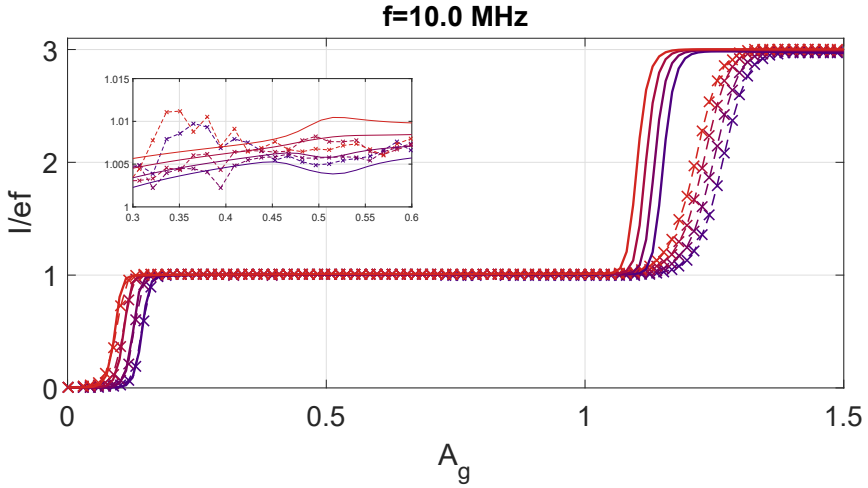

Figure 33: The measured pumping data for sample B at 10 MHz.

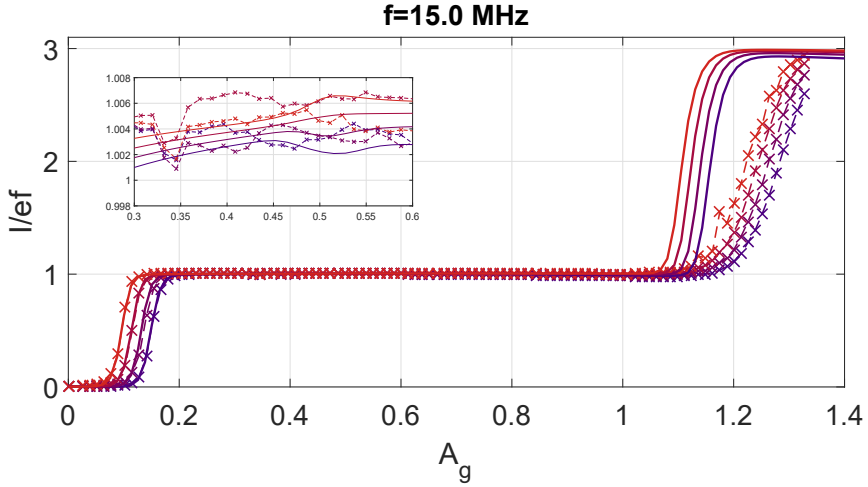

Figure 34: The measured pumping data for sample B at 15 MHz.

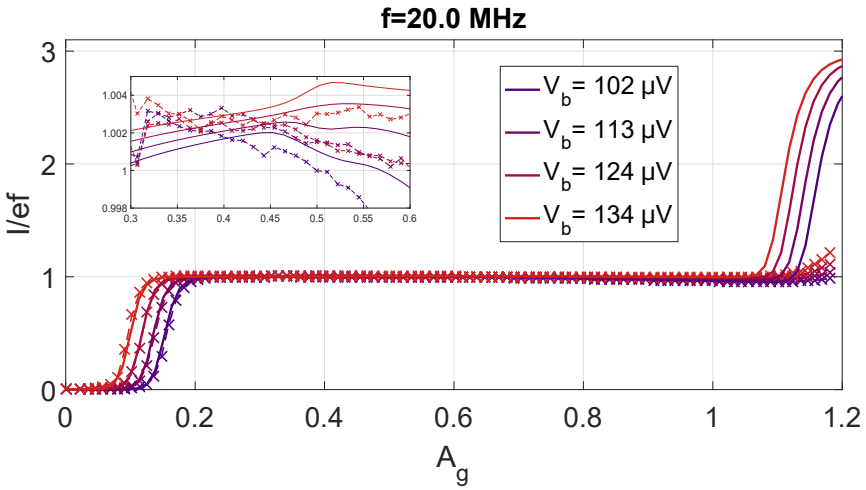

Figure 35: The measured pumping data for sample B at 20 MHz.

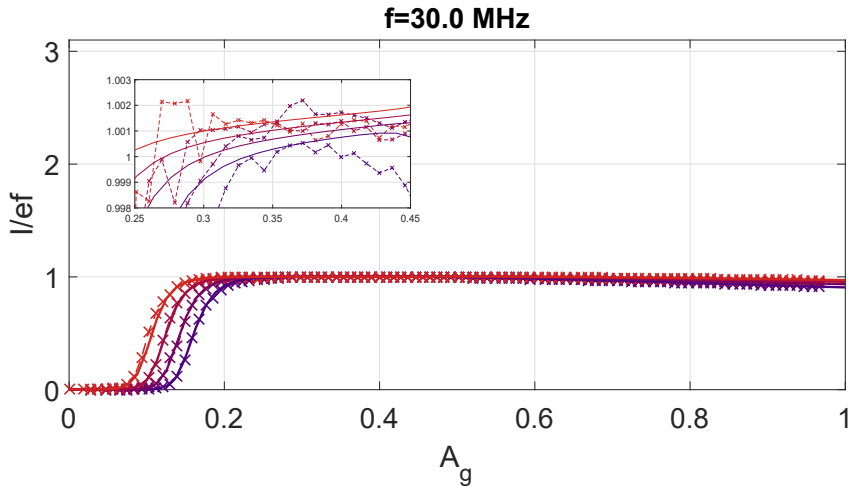

Figure 36: The measured pumping data for sample B at 30 MHz.

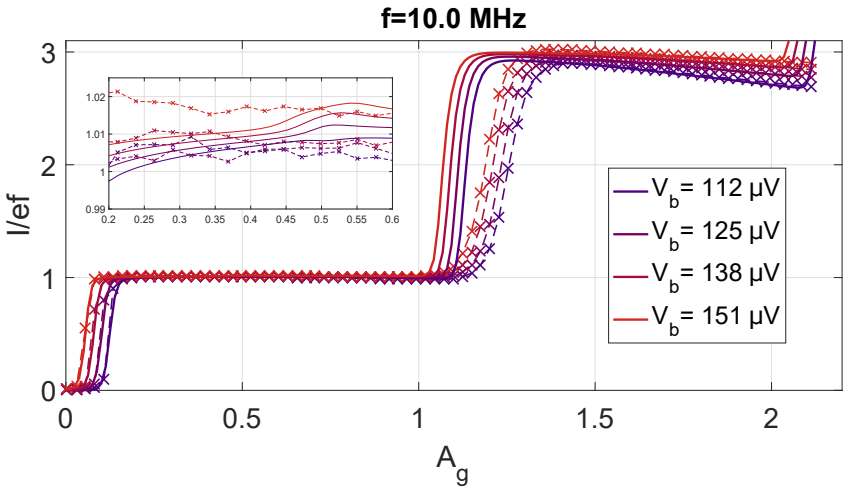

Figure 37: The measured pumping data for sample C at 10 MHz.

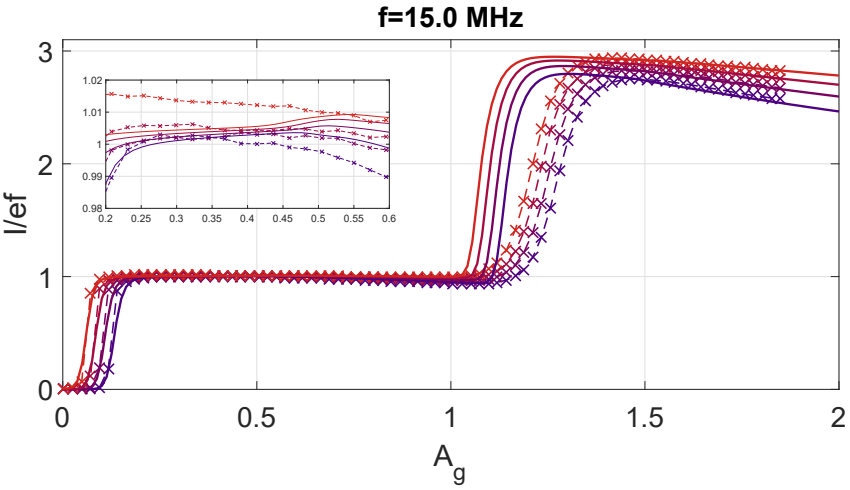

Figure 38: The measured pumping data for sample C at 15 MHz.

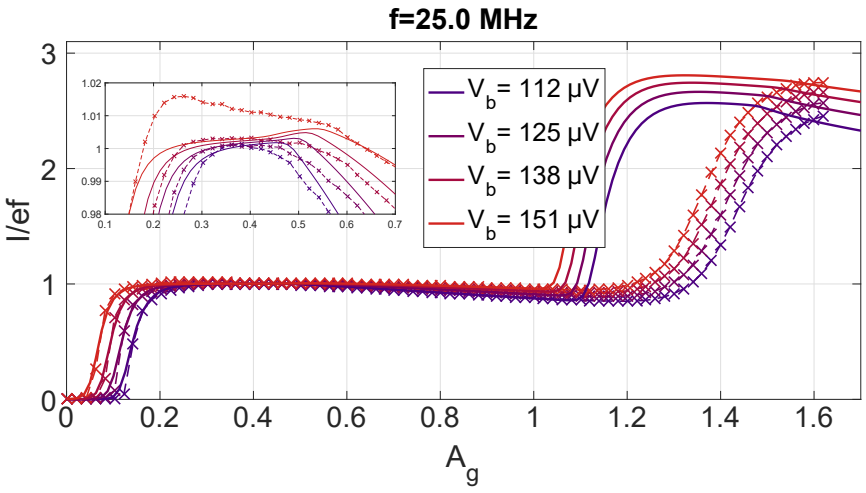

Figure 39: The measured pumping data for sample C at 25 MHz.

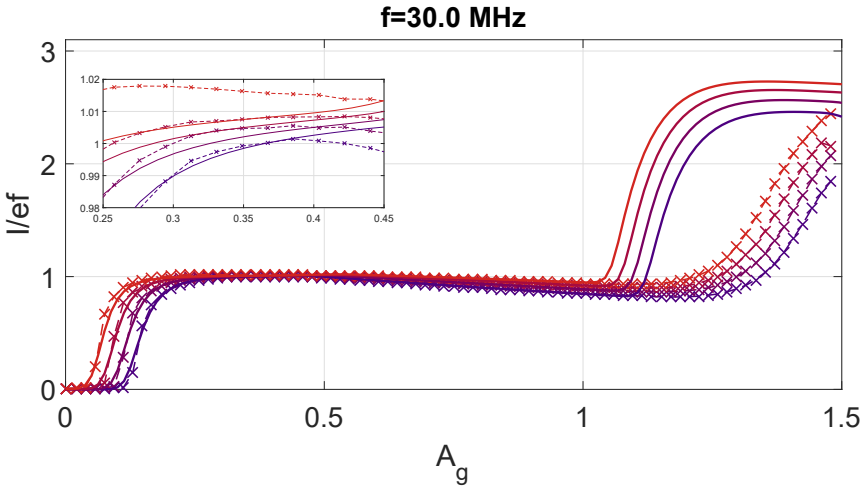

Figure 40: The measured pumping data for sample C at 30 MHz.

In figures 32–40 we present the pumping data for samples B and C. We observe that the data is much noisier for these two samples. This is largely because we had to exclude a significant amount of pumping experiments from the averaging. Furthermore, in this cooldown the overall low-frequency noise was larger compared to sample A and later experiments. Due to the noise, it is impossible to reliably extract the temperature of the superconducting leads from the experimental data, since e.g. in fig. 33 it can be seen that the noise itself may be greater than the spreading of the pumping plateau in the simulations. We also observe that the onset of the pumping plateau corresponding to current output of $3ef$ is not particularly steep. This may be caused by drift in the dc part of the gate drive, in which case the gate drive does not occur around the degeneracy

point. As a results, the onset occurs at higher amplitudes, as can be seen in fig. 5. For this measurement, we did not save the gate modulations obtained during the automated estimation of the dc voltage corresponding to $n_{g0} = 1/2$. This source of uncertainty was fixed in subsequent measurements.

5.3 Quasiparticle density

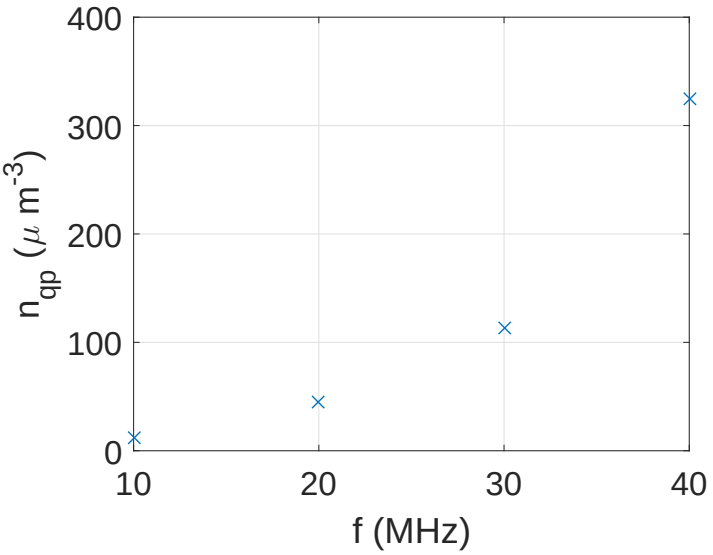

Figure 41: Quasiparticle density calculated from the estimated temperatures for sample A.

In fig. 41 we present the quasiparticle density estimates based on the temperatures used to fit the pumping data for sample A. For sample B and C we were not able to extract a temperature dependence due to the bad quality of the data. For sample A, we have estimated significantly larger quasiparticle densities than in previous experiments with similiar sample geometry [49]. However, in this experiment the resistances of the samples measured were an order of magnitude smaller than in the experiments discussed in this thesis. For a given bias range, having a smaller tunneling resistance leads to a larger leakage current, resulting in a wider spread of the pumping plateaus, which makes temperature estimates easier. Since samples B and C had an even larger tunneling resistance, estimating the temperature is even harder.

6 Summary and discussion

In the work presented in this thesis, we have fabricated hybrid single electron turnstiles with two different lead geometries and significantly different thicknesses in order to study the effects of lead thickness and geometry on the density of non-equilibrium quasiparticles during turnstile operation.

The advantage in using superconducting leads with a higher thickness is that the diffusion of the quasiparticles away from the tunnel junctions is more efficient, resulting in an overall smaller quasiparticle density near the junction. Reducing the quasiparticle density is essential in reaching accuracies required for metrological applications.

We present the first experimental demonstration of charge pumping with Al/AlMn turnstiles with a junction quality comparable to conventional Al/Cu structures. However, we were not able to quantitatively observe the predicted improvements on the turnstile performance based on the better thermalization of the superconducting leads. Our initial analysis of the experiments suggested significantly larger quasiparticle densities for our samples with thin aluminum leads compared to quasiparticle densities observed in previous experiments. For the samples with very thick aluminum leads, we were not able to extract any kind of temperature dependence due to the low quality of the experimental data.

Despite the shortcomings in the experiments, we were able to fabricate SINIS turnstiles with charging energy exceeding the superconducting gap with very thick aluminum leads. We noted that at these thicknesses the superconducting gap approaches its bulk value, which is lower than for thin films. Low superconducting gap deteriorates the performance the device. Building on our demonstrations of AlMn based devices, in future work this issue might be addressed by using some other metal as the superconductor, e.g. niobium or vanadium. Aluminum is typically chosen as the superconductor because it can easily be oxidised in order to fabricate the tunnel barriers. With the fabricating methods we have used, this is not an issue since we oxidise the normal metal instead of the superconductor. However, niobium-based junctions typically have a larger value for the Dynes parameter γ. [50]

In order to verify whether having thicker leads decreases the quasiparticle density, more experiments are required. There is, however, plenty of room for improvement in the sample fabrication process. The most important parameter to improve is the tunneling resistance of the samples, which can be made an order of magnitude smaller. The resistance is determined by the junction size and the oxidation conditions. Increasing the junction size also increases the capacitance of the junctions, which leads to a smaller charging energy and therefore the most feasible way to tune the resistance is by changing the oxidation parameters. In our sample fabrication process, the oxidation time was of the order of minutes, which means that it can easily be decreased.

References

1. *The International System of Units (SI)* <http://www.bipm.org/en/publications/si-brochure/> (2006).
2. Vigoureux, P. A Determination of the Ampere. *Metrologia* **1,** 3 (1965).
3. Griffiths, D. *Introduction to Electrodynamics* (Prentice Hall, 1999).
4. Ahlers, F. J. & Siegner, U. *The redefinition of the ampere* Proceedings from the 56th International Scientific Colloquium. 2011.
5. Josephson, B. D. Possible new effects in superconductive tunnelling. *Physics Letters* **1,** 251 (1962).
6. Laughlin, R. B. Quantized Hall conductivity in two dimensions. *Physical Review B* **23,** 5632 (1981).
7. Likharev, K. K., Bakhvalov, N. S., Kazacha, G. S. & Serdyukova, S. I. Single-electron tunnel junction array: an electrostatic analog of the Josephson transmission line. *IEEE Transactions on Magnetics* **25,** 1436 (1989).
8. Pekola, J. P. *et al.* Single-electron current sources: Toward a refined definition of the ampere. *Review of Modern Physics* **85,** 1421 (2013).
9. Geerligs, L. J. *et al.* Single Cooper pair pump. *Zeitschrift für Physik B Condensed Matter* **85,** 349 (1991).
10. Niskanen, A. O., Pekola, J. P. & Seppä, H. Fast and Accurate Single-Island Charge Pump: Implementation of a Cooper Pair Pump. *Physical Review Letters* **91,** 177003 (2003).
11. Nagamune, Y. *et al.* Single electron transport and current quantization in a novel quantum dot structure. *Applied Physics Letters* **64,** 2379 (1994).
12. Fujiwara, A., Nishiguchi, K. & Ono, Y. Nanoampere charge pump by single-electron ratchet using silicon nanowire metal-oxide-semiconductor field-effect transistor. *Applied Physics Letters* **92,** 042102 (2008).
13. Giblin, S. P. *et al.* Towards a quantum representation of the ampere using single electron pumps. *Nature Communications* **3,** 930 (2012).
14. Fulton, T. A. & Dolan, G. J. Observation of single-electron charging effects in small tunnel junctions. *Physical Review Letters* **59,** 109 (1987).
15. Geerligs, L. J. *et al.* Frequency-locked turnstile device for single electrons. *Physical Review Letters* **64,** 2691 (1990).
16. Keller, M. W., Martinis, J. M., Zimmerman, N. M. & Steinbach, A. H. Accuracy of electron counting using a 7-junction electron pump. *Applied Physics Letters* **69,** 1804 (1996).
17. Keller, M. W., Eichenberger, A. L., Martinis, J. M. & Zimmerman, N. M. A Capacitance Standard Based on Counting Electrons. *Science* **285,** 1706 (1999).

18. Pekola, J. *et al.* Hybrid single-electron transistor as a source of quantized electric current. *Nature Physics* **4,** 120 (2008).

19. Maisi, V. F., Pashkin, Y. A., Kafanov, S., Tsai, J.-S. & Pekola, J. P. Parallel pumping of electrons. *New Journal of Physics* **11,** 113057 (2009).

20. Court, N. A., Ferguson, A. J., Lutchyn, R. & Clark, R. G. Quantitative study of quasiparticle traps using the single-Cooper-pair transistor. *Physical Review B* **77,** 100501 (2008).

21. Taupin, M., Khaymovich, I. M., Meschke, M., Mel'nikov, A. S. & Pekola, J. P. Tunable quasiparticle trapping in Meissner and vortex states of mesoscopic superconductors. *Nature Communications* **7,** 10977 (2016).

22. Scherer, H. & Camarota, B. Quantum metrology triangle experiments: a status review. *Measurement Science and Technology* **23,** 124010 (2012).

23. Van Delft, D. & Kes, P. The discovery of superconductivity. *Physics Today* **63,** 38 (2010).

24. Bardeen, J., Cooper, L. N. & Schrieffer, J. R. Microscopic Theory of Superconductivity. *Physical Review* **106,** 162 (1957).

25. Tinkham, M. *Introduction to Superconductivity: Second Edition* (Dover Publications, 2004).

26. Grabert, H. & Devoret, M. *Single Charge Tunneling - Coulomb Blockade Phenomena In Nanostructures* (Plenum Press, 1992).

27. Pekola, J. P. *et al.* Environment-Assisted Tunneling as an Origin of the Dynes Density of States. *Physical Review Letters* **105,** 026803 (2010).

28. Aref, T., Maisi, V. F., Gustafsson, M. V., Delsing, P. & Pekola, J. P. Andreev tunneling in charge pumping with SINIS turnstiles. *Europhysics Letters* **96,** 37008 (2011).

29. Greibe, T. *et al.* Are "Pinholes" the Cause of Excess Current in Superconducting Tunnel Junctions? A Study of Andreev Current in Highly Resistive Junctions. *Physical Review Letters* **106,** 097001 (2011).

30. Saira, O.-P., Kemppinen, A., Maisi, V. F. & Pekola, J. P. Vanishing quasiparticle density in a hybrid Al/Cu/Al single-electron transistor. *Physical Review B* **85,** 012504 (2012).

31. Tinkham, M. & Clarke, J. Theory of Pair-Quasiparticle Potential Difference in Nonequilibrium Superconductors. *Physical Review Letters* **28,** 1366 (1972).

32. Maisi, V. F. *Andreev Tunneling and Quasiparticle Excitations in Mesoscopic Normal Metal - Superconductor Structures* PhD thesis (Aalto University School of Science, 2014).

33. Sillanpää, M. A., Heikkilä, T. T., Lindell, R. K. & Hakonen, P. J. Inverse proximity effect in superconductors near ferromagnetic material. *Europhysics Letters* **56,** 590 (2001).

34. Bardeen, J., Rickayzen, G. & Tewordt, L. Theory of the Thermal Conductivity of Superconductors. *Physical Reviews* **113,** 982 (1959).

35. Dolan, G. J. Offset masks for lift-off photoprocessing. *Applied Physics Letters* **31,** 337 (1977).

36. Pekola, J. P. *et al.* Environment-Assisted Tunneling as an Origin of the Dynes Density of States. *Physical Review Letters* **105,** 026803 (2010).

37. <http://www.allresist.com/csar-62-ar-p-6200/>.

38. George, S. M. Atomic Layer Deposition: An Overview. *Chemical Reviews* **110,** 111 (2010).

39. O'Neil, G. C., Schmidt, D. R., Tomlin, N. A. & Ullom, J. N. Quasiparticle density of states measurements in clean superconducting AlMn alloys. *Journal of Applied Physics* **107,** 093903 (2010).

40. Moore, D. C *et al.* Quasiparticle trapping in Microwave Kinetic Inductance Strip Detectors. *AIP Conference Proceedings* **1185,** 168 (2009).

41. Nguyen, H. Q. *et al.* Trapping hot quasi-particles in a high-power superconducting electronic cooler. *New Journal of Physics* **15,** 085013 (2013).

42. Pobell, F. *Matter and Methods at Low Temperatures* (Springer, 2007).

43. Kemppinen, A. *et al.* Long hold times in a two-junction electron trap. *Applied Physics Letters* **99,** 142106 (2011).

44. Zorin, A. B. The thermocoax cable as the microwave frequency filter for single electron circuits. *Review of Scientific Instruments* **66,** 4296 (1995).

45. <http://www.keysight.com/en/pd-2155053-pn-33522B/waveform-generator-30-mhz-2-channel-with-arb>.

46. <http://www.femto.de/en/products/current-amplifiers/sub-femto-ampere-var-gain-ddpca/30-variable-gain-sub-femto-ampere-current-amplifier-ddpca-300>.

47. Chupov, P. N., Eremenko, V. V & Pilipenko, Y. A. Dependence of the Critical Temperature and Energy Gap on the Thickness of Superconducting Aluminum Films. *Journal of Experimental and Theoretical Physic* **28,** 752 (1969).

48. Kittel, C. *Introduction to Solid State Physics* (Wiley, 2004).

49. Knowles, H. S., Maisi, V. F. & Pekola, J. P. Probing quasiparticle excitations in a hybrid single electron transistor. *Applied Physics Letters* **100,** 262601 (2012).

50. Nevala, M. *Development of niobium-based superconducting junctions* PhD thesis (University of Jyväskylä, 2012).